Journal of Extracellular Biology

RESEARCH ARTICLE OPEN ACCESS

Extracellular Vesicle Properties and Functions Are Defined by the Originating Cell's Fitness Status

Stephanie Leyk[1,2] | Imke Liebold[1,2] | Clarissa Lanzloth[1,2] | Ulricke Richardt[2] | Johan M. Kux[3] | Christoph Kilian[1] | Manuela Moritz[4] | Antonia Gocke[4,5,6] | Simon Meyer[1,7] | Katharina Höhn[8] | Barbara Honecker[9] | Helmut Haas[10] | Marius Böttcher[1] | Sören Weidemann[11] | Simon Kind[11] | Hartmut Schlüter[4] | Nahla Galal Metwally[12] | Lorenz Adlung[1,13] | Pablo J. Sáez[3] | Thomas Jacobs[2] | Klaus Ruckdeschel[14] | Lidia Bosurgi[1,2]

[1]I. Department of Medicine, University Medical Center Hamburg-Eppendorf (UKE), Hamburg, Germany | [2]Protozoa Immunology, Bernhard-Nocht-Institute for Tropical Medicine (BNITM), Hamburg, Germany | [3]Cell Communication and Migration Laboratory, Institute of Biochemistry and Molecular Cell Biology, Center for Experimental Medicine, University Medical Center Hamburg-Eppendorf (UKE), Hamburg, Germany | [4]Section/Core Facility Mass Spectrometry and Proteomics, Center for Diagnostics, University Medical Center Hamburg–Eppendorf (UKE), Hamburg, Germany | [5]Center for Molecular Neurobiology Hamburg (ZMNH), University Medical Center Hamburg-Eppendorf (UKE), Hamburg, Germany | [6]Institute of Neuropathology, University Medical Center Hamburg-Eppendorf (UKE), Hamburg, Germany | [7]Institute of Biochemistry and Molecular Cell Biology, University Medical Center Hamburg-Eppendorf (UKE), Hamburg, Germany | [8]Cellular Parasitology Department, Bernhard-Nocht-Institute for Tropical Medicine (BNITM), Hamburg, Germany | [9]Molecular Infection Immunology, Bernhard-Nocht-Institute for Tropical Medicine (BNITM), Hamburg, Germany | [10]*helminGuard*, Sülfeld/Borstel, Germany | [11]Institute of Pathology with the sections Molecular Pathology and Cytopathology, University Medical Center Hamburg-Eppendorf (UKE), Hamburg, Germany | [12]Research Group Host-Parasite Interaction, Bernhard-Nocht-Institute for Tropical Medicine (BNITM), Hamburg, Germany | [13]Hamburg Center for Translational Immunology (HCTI) & Center for Biomedical AI (bAIome), University Medical Center Hamburg-Eppendorf (UKE), Hamburg, Germany | [14]Institute of Medical Microbiology, Virology and Hygiene, University Medical Center Hamburg-Eppendorf (UKE), Hamburg, Germany

Correspondence: Lidia Bosurgi (l.bosurgi@uke.de)

Received: 5 May 2025 | **Revised:** 14 December 2025 | **Accepted:** 14 January 2026

Keywords: apoptosis | apoptotic bodies | extracellular vesicles | macrophages | schistosomiasis

ABSTRACT

Recent studies have focused on the role of dying cells in modulating immune function and shaping the local microenvironment. Apoptotic cells release various extracellular vesicles (EVs), such as exosomes and microvesicles, and form apoptotic bodies through membrane blebbing. Despite growing interest in EVs, the effects of EVs derived from apoptotic cells versus those from live cell remain poorly understood.

Here, via transmission electron microscopy, nanoparticle tracking analysis, proteomics, and flow cytometry, we characterise the distinct features of EVs from live versus apoptotic cells. Using a model of *Schistosoma mansoni* infection, characterised by the presence of dying cells due to parasite egg accumulation, we demonstrate that the injection of apoptotic T cell-derived EVs attenuates hepatocyte damage, in contrast to EVs from live T cells.

Analysis of the transcriptomic profile of target macrophages and functional assays revealed that apoptotic cell-derived EVs activate nitric oxide-related pathways, which modulate macrophage function. Furthermore, these EVs specifically promoted fibroblast-mediated wound healing in vitro.

Collectively, our findings highlight that cell fitness influences EV properties and their immune regulatory function. Investigating the differences between EVs from living and apoptotic cells is essential for advancing our understanding of immune regulation and optimising the development of EV-based therapeutic strategies.

1 | Introduction

Apoptosis is a programmed form of cell death that occurs during development, ageing and in response to tissue damage. By modulating the immune response, it serves as a defence mechanism against pathogens and damaged cells (Kerr et al. 1972; Norbury and Hickson 2001; Nössing and Ryan 2023). Besides the release of common types of extracellular vesicles (EVs) such as exosomes and microvesicles, cells undergoing apoptosis are characterised by membrane blebbing, resulting in the release of apoptotic bodies, which are considered one of the largest types of EVs (van Niel et al. 2018). Their biogenesis is initiated by caspases activated by the apoptosis pathway, which contribute to apoptotic body formation and cargo packaging (Bratton et al. 1997; Enari et al. 1998; Mandal et al. 2005; Segawa et al. 2014). Like EVs released by live cells, EVs released by apoptotic cells (ApoEVs), contain diverse cargos such as DNA, RNA, proteins, and lipids. Notably, ApoEVs can also contain whole mitochondria, ribosomes or fragments of those organelles (Kerr et al. 1972; van Niel et al. 2018). These cargos play a crucial role in modulating cell-to-cell communication during health and disease. By acting as chemoattractants and amplifiers of eat-me signals (Pontejo and Murphy 2021), as well as through the recognition of specific CASPASE-3-induced glycosylation patterns (Bilyy et al. 2012), ApoEVs have been described as contributing to phagocytes' clearance of apoptotic corpses (Pontejo and Murphy 2021). Their immunomodulatory functions have been shown to range from regenerative to pro-inflammatory, most likely determined by their cellular origin: Whereas ApoEVs derived from mesenchymal stem cells support liver regeneration and protect against acute hepatic failure (Sui et al. 2021), ApoEVs from apoptotic lymphoblasts contain autoantigens such as histones and DNA, which are suggested to contribute to the pathogenicity of autoimmune diseases, such as systemic lupus erythematosus (Cocca et al. 2002). These data have proven that, in contrast to the long-standing perception, ApoEVs are not merely cell junk packaged into edible portions for clearance by phagocytes but actively have the properties to influence intercellular communication (Caruso and Poon 2018). However, the molecular and functional features that distinguish these EVs from those produced by viable cells remain largely unexplored and warrant further investigation.

Macrophages (Mφs) are extensively studied as targets of EVs, as EVs have the potential to influence Mφ polarisation status and are thus an important part of the immune response. Their effect on Mφ polarisation is highly dependent on the cellular source of the EVs. Mesenchymal stromal cells-derived EVs, for example, mediate anti-inflammatory effects such as the release of TGF-β and IL-10, promoting tissue repair (Ti et al. 2015), whereas EVs from cardiomyocytes promote the release of pro-inflammatory cytokines (TNF, IL-1β, IL-6) and nitric oxide (NO) and thus a pro-inflammatory Mφ response (Yarana et al. 2019). Besides EV sensing, Mφs play a key role in maintaining tissue homeostasis and initiating a wound-healing response by sensing and clearing apoptotic cells (Bosurgi et al. 2017; Schilperoort et al. 2023; Zhang et al. 2019). During infection with the parasitic trematode *Schistosoma mansoni*, premature T-cell death, mediated by IL-10, has been described as one of the factors contributing to the Th1/Th2 switch—a key feature of the immune response generated upon infection with the parasite (Estaquier et al. 1997). Additionally, we have recently described that apoptotic cell clearance by Mφs critically determines the *S. mansoni* infection outcome, with the uptake in vivo of apoptotic neutrophils and T cells by hepatic monocytes/Mφs being essential for parasitic egg clearance (Liebold et al. 2024). In this scenario, EVs released by the pathogen itself and by host cells have been shown to mediate cellular signalling and thereby influence disease pathogenesis by contributing to Mφ polarisation and the development of fibrosis (Qi et al. 2023; L. Wang et al. 2022; Y. Wang et al. 2022). Yet, the role of ApoEVs in this setting has not been addressed so far.

In this study, we investigate the different characteristics and functions of EVs released by live and ApoEVs, both in vitro and during the acute phase of *S. mansoni* infection. Our findings show that the injection of ApoEVs ameliorates hepatocyte damage during *S. mansoni* infection. Additionally, ApoEVs exhibit unique features compared to those from live cells, notably their ability to induce NO-related pathways in target Mφs.

These data underscore the relevance of considering ApoEVs as a tool to influence target cell activation and highlight the potential of EVs to mitigate liver damage during *S. mansoni* infection.

2 | Methods

2.1 | Mice

Wild-type C57BL/6J mice were bred and maintained in a specific pathogen-free facility at the BNITM. All animal experiments were approved by the Office for Consumer Protection of the city of Hamburg (experiment protocol N105/2021, organ harvesting protocols 2021/T001 and 2018/T006). For in vivo experiments, 8- to 12-week-old male and female mice were used, and for in vitro experiments, 8- to 14-week-old mice were used.

2.2 | Isolation of Liver-Derived EVs

Livers were perfused using 0.2-µm filtered PBS, collected, and minced into small pieces. The digestion medium, consisting of DMEM (PAN Biotech), 1 mg/mL Collagenase IV (Gibco), 1% $MgCl_2$ (0.2 M), 0.4% $CaCl_2$ (0.5 M) and 0.5% DNase I (150 U/mL), was filtered through a 0.2-µm syringe filter. 10 mL of the filtered medium were added to the minced cells, followed by incubation for 45 min at 37°C with shaking. The digested cell suspension was filtered through a 70-µm cell strainer and centrifuged at 300 rcf for 5 min. The supernatant containing EVs was kept and cleared from debris by further washing steps for 5 min at 300 rcf, 20 min at 2000 rcf and 45 min at 16,000 rcf. Each washing step was repeated at least twice. EVs were pelleted from the supernatant after the last 16,000 rcf washing step at 100,000 rcf for 1 h. The pellet was resuspended in 0.2-µm filtered PBS and washed at 100,000 rcf for 1 h. The 100,000 rcf EV pellet (corresponding to the material pelleted at 100,000× rcf) was resuspended in various amounts of 0.2-µm filtered PBS or other reagents depending on the following experimental uses.

2.3 | Isolation of Liver Cells

Livers were perfused with PBS through the vena cava and collected. On a petri dish, livers were minced into small pieces, transferred into digestion media containing 10-mL DMEM (PAN Biotech) containing 1 mg/mL Collagenase IV (Gibco), 1% $MgCl_2$ (0.2 M), 0.4% $CaCl_2$ (0.5 M) and 0.5% DNase I (150 U/mL) and incubated for 45 min at 37°C while shaking. To obtain a single-cell suspension, the digested tissue pieces were mashed through a 70-µm cell strainer and washed multiple times with PBS containing 2% FCS at 300 rcf for 5 min at 4°C. The suspension was centrifuged at 50 rcf for 4 min, the supernatant was transferred into a new falcon, washed, and the non-parenchymal cells were resuspended in 6 mL 37% Percoll. Cells were centrifuged for 10 min at 400 rcf (deceleration 1/ acceleration 9), and a red blood cell lysis of the pellet was performed, followed by washing with PBS containing 2% FCS. The cells were kept on ice and further processed for downstream analysis.

2.4 | Flow Cytometry of Cells

Cells harvested from culture plates (e.g., bone marrow-derived macrophages [BMDMs], hepatocytes and fibroblasts) or isolated from mouse livers were incubated with anti-CD16/CD32 diluted 1:10,000 in PBS + 2% FCS for 15 min at 4°C prior to the staining. For the labelling of surface epitopes, cells were incubated with the selected antibodies for 45 min at 4°C in the dark as reported in Table 1. If intracellular epitopes were analysed on BMDMs, hepatocytes and fibroblasts, cells were fixed using 2% PFA and permeabilised using perm/wash buffer (BD Bioscience) for 15 min at RT before staining, whereas cells isolated from the liver were fixed and permeabilised using the Foxp3 staining Kit (eBioscience) and permeabilisation buffer (BD Bioscience) according to the manufacturer's instructions. Cells were acquired on an Aurora (Cytek) flow cytometer, and data were analysed using FlowJo V10. Mean fluorescence intensity (MFI) was calculated from the median; negative values were excluded.

2.5 | Transmission Electron Microscopy (TEM)

A 50-µL aliquot of freshly isolated EVs was fixed with 5% glutaraldehyde. Then 20 µL of EVs were incubated on carbon-coated and glow-discharged copper grids (Science Services, München, Germany) for 20 min. Afterwards, the grids were blotted and washed once with water. The grids were subsequently stained with 2% Uranylacetate (Electron Microscopy Sciences, Hatfield, USA) for 15 s and allowed to dry for 30 min. Finally, the EVs were analysed by TEM (BNITM Hamburg, Germany) via a Tecnai Spirit electron microscope (Thermo Fisher Scientific, Waltham, USA) operating at 80 kV, and images were recorded with a digital CCD camera.

2.6 | Nanoparticle tracking analysis (NTA)

Size and concentration of EV samples were measured by NTA with the Nanosight LM14C equipped with a CCD camera (Malvern Panalytical). Initially, 500 µL of EV suspension was injected into the chamber, and each sample was measured 5 times for a recording time of 30 s. Between every measurement, 100 µL of fresh EV suspension was injected. The camera level was set to 12, the screen gain was set to 10.00, and the temperature control was set at 25°C.

2.7 | Western Blot

For the western blot analysis of EVs, EV pellets have been lysed with RIPA buffer (50-mM Tris-HCl pH 7.4; 5-mM EDTA; 150-mM NaCl; 1-mM Na-pyrophosphate; 1-mM NaF; 1-mM Na-vanadate; 1% NP-40) supplemented with a complete, Mini, EDTA-free Protease Inhibitor Cocktail (Roche) using TissueLyser-type3 (QIAGEN; 20 Hz for 2 × 3 min) after the last centrifugation step of the EV isolation.

For the western blot analysis of tissues, a section of liver stored in RNAprotect Tissue Reagent (Qiagen, Hilden, Germany) was homogenised in 10× (v/w) RIPA buffer (50-mM Tris-HCl pH 7.4; 5-mM EDTA; 150-mM NaCl; 1-mM Na-pyrophosphate; 1-mM NaF; 1-mM Na-vanadate; 1% NP-40) supplemented with the complete Mini Protease Inhibitor (Roche) using TissueLyser-type3 (QIAGEN; 20 Hz for 2 × 3 min). Samples were centrifuged for 10 min at 13,000 g and 4°C, and the supernatant was collected without contamination from the upper lipid layer.

Protein concentration was determined via the bicinchoninic acid assay (BCA). Samples were diluted in RIPA buffer and twofold NuPAGE LDS Sample buffer with a sample reducing agent (Invitrogen). For cells isolated from liver tissue, 50 µg of total protein was loaded; for EVs isolated from thymocytes and corresponding liveT and aT controls, 2.5 µg of total protein was loaded; and for EVs isolated from liver tissue and corresponding liveT and aT controls, 15 µg of total protein was loaded. Proteins were separated in 10% Tris-glycine SDS-PAGE and transferred to nitrocellulose membranes (GE Healthcare) using a wet blotting system (blotting buffer: 20-mM Tris, 150-mM glycine, 20% (v/v) methanol) overnight at 200 mA. Membranes were stained with Ponceau Red (Sigma), cut and blocked for 1 h in 5% milk in TBS-T (20-mM Tris, 150-mM NaCl, 0.1% (v/v) Tween 20). Membranes were incubated overnight at 4°C with the corresponding primary antibodies (listed in Table 2) diluted 1:1000 in 5% BSA (Sigma) in TBS-T. After washing 3 × 10 min in TBS-T, membranes were incubated for 1 h at RT with the corresponding HRP-conjugated secondary antibody diluted 1:5000 in 5% milk in TBS-T. After washing 3 × 10 min in TBS-T, the proteins of interest were detected with the Amersham Imager 600 (GE Healthcare) using SuperSignal West Femto ECL (Thermofisher). Protein quantification was performed using ImageJ 1.54 g.

2.8 | Protein Concentration

Protein concentration of EV samples was determined using the Qubit protein assay kit (Invitrogen) according to the manufacturer's instructions. Briefly, 1 µL of protein reagent was added to 199 µL of protein buffer for reconstitution of the working solution. A working solution of 190 µL was added to the 10 µL of sample or standard in a Qubit tube, vortexed and measured with the Qubit 4 fluorometer.

TABLE 1 | List of antibodies and dyes used for flow cytometry.

Epitope/antibody	Fluorochrome	Clone	Amount/dilution	Manufacturer
a-goat IgG	FITC	CHXGO	1:200	Invitrogen, Carlsbad (USA)
Annexin V	FITC	/	1 µL	Biolegend, San Diego (USA)
Arg1	APC	AlexF5	1:500	Invitrogen, Carlsbad (USA)
B220	PE-Cy5	RA3-6B2	1:300	BD Bioscience, Heidelberg (Germany)
CD3	PE BUV395	17A2 145-2C11	1 µL 1:200	Biolegend, San Diego (USA) BD Bioscience, Heidelberg (Germany)
CD4	PE	RM4	1 µL	Biolegend, San Diego (USA)
CD8	PE	53-6.7	1 µL	Biolegend, San Diego (USA)
CD9	PE-Dazzle	MZB	1 µL	Biolegend, San Diego (USA)
CD11b	PE APC-Cy7	M1/70	1 µL 1:400	Biolegend, San Diego (USA)
CD11c	PE	N418	1 µL	Biolegend, San Diego (USA)
CD44	PE	1M7	1 µL	Biolegend, San Diego (USA)
CD45	APC	30-F11	1 µL/ 1:500	Biolegend, San Diego (USA)
CD49b	PE	Dx5	1 µL	Biolegend, San Diego (USA)
CD64	BV605	X54-5/7.1	1:300	Biolegend, San Diego (USA)
CFDA SE	/	/	1:1500	ThermoFisher Scientific, Waltham (USA)
Cleaved CASPASE-3	AF647	D3E9	1 µL	Cell Signaling Technology, Danvers (USA)
F4/80	AF700	BM8	1:400	Biolegend, San Diego (USA)
iNOS	eFluor450	LXNFT	1:250	Invitrogen, Carlsbad (USA)
Ki67	BV650	11F6	1:100	Biolegend, San Diego (USA)
Ly6C	PerCP-Cy5.5	HK1.4	1:300	Biolegend, San Diego (USA)
Ly6G	BV421	1A8	1:500	Biolegend, San Diego (USA)
MERTK	PE	12310C42	1:300	Biolegend, San Diego (USA)
MHC-I	PE BV510	SF1-1.1.1	1 µL	eBioscience, Frankfurt am Main (Germany)
MHC-II	PE PerCP	M51114.15.2	1 µL	eBioscience, Frankfurt am Main (Germany)
Proprium iodide solution	/	/	0.5 µL	Biolegend, San Diego (USA)
SiglecF	BV421	S17007L	1:300	Biolegend, San Diego (USA)
a-mCh13L3 (Ym1)	/	ECF-L	1:200	R&D Systems, Minneapolis (USA)

2.9 | MACSPlex

The MACSPlex (Miltenyi Biotec) was used according to the manufacturer's instructions. Briefly, 15-µL capture beads were added to 20-µg EVs (for T-EVs: 10-µg small EVs + 10-µg large EVs) or buffer control, resuspended in 200-µL MACSPlex buffer and incubated at RT on an orbital shaker protected from light overnight. Samples were washed with 500-µL MACSPlex buffer at 3000 rcf for 5 min at RT. About 5 µL per detection reagent were added to the pellet and incubated for 1 h at RT on an orbital shaker protected from light. Samples were washed, the pellet was resuspended in 500-µL MACSPlex buffer and incubated for 15 min at RT on an orbital shaker protected from light. After a final step of centrifugation, samples were resuspended in 200-µL MACSPlex buffer, acquired at the Accuri C6 and analysed using FlowJo V10.

TABLE 2 | List of primary antibodies used for western blot.

Antibody	Company (cat. number)
GM130	Cell Signaling (70767)
TSG101	Cell Signaling (72312)
Histone H3	Cell Signaling (9715)
γ-Tubulin	Abcam (ab179503)
CASPASE-3 (total)	Cell Signaling (9662S)
Cleaved CASPASE-3 (Asp175) (5A1E)	Cell Signaling (9664S)
Cleaved PARP (Asp214) (7C9)	Cell Signaling (9548T)

2.10 | Isolation of Thymocytes and Induction of Apoptosis

Thymuses were harvested from naïve mice and smashed over a 40-µm strainer to obtain a single-cell solution. Cells were washed with 0.2-µm filtered PBS and plated in a petri dish in RPMI containing 5% FCS and 0.5% Gentamycin. The medium was previously depleted from EVs via centrifugation at 100,000 rcf for 16 h and sterile filtration over a 0.2-µm filter. Cells and supernatant were harvested after 1–3 h and centrifuged at 300 rcf for 5 min. The supernatant was collected for the isolation of EVs from live thymocytes (liveT-EVs); 10 µL of the cells were used for the detection of apoptosis rates, and the remaining cells were resuspended in a 10-mL medium and transferred back into the petri dish. For the induction of apoptosis, cells were kept in culture for additional 24 h at 37°C and 5% CO_2. Cells and supernatant were harvested as described above. The supernatant was used for the isolation of EVs from apoptotic thymocytes (aT-EVs). The apoptosis rates were determined using the FITC Annexin V Apoptosis Detection Kit with PI (Biolegend). Briefly, 100 µL of Annexin V binding buffer and 1 µL of Annexin V were added to 10 µL of cell suspension and incubated for 15 min at RT in the dark. In addition, 100 µL of Annexin V binding buffer and 0.5 µL of PI were added and samples were immediately measured at the LSR II flow cytometer.

2.11 | EV Isolation From Thymocytes

The supernatants of live or apoptotic thymocytes were generated as described above. To isolate EVs via differential centrifugation, the supernatants were first cleared from cells and debris by centrifugation 2× at 300 rcf for 5 min and 2× at 2000 rcf for 20 min, transferring the supernatant into a new tube after each step. Large EVs were isolated from the remaining supernatant via centrifugation at 16,000 rcf for 45 min. The pellet was resuspended in 0.2 µm of filtered PBS and repeatedly centrifuged at 16,000 rcf (16,000 rcf pellet defined through the text as large EVs). The supernatant was transferred into a fresh tube and centrifuged at 100,000 rcf for 1 h to isolate small EVs (100,000 rcf pellet defined through the text as small EVs). The pellet was resuspended in 0.2-µm filtered PBS and repeatedly centrifuged at 100,000 rcf. All centrifugation steps were performed at 4°C. Centrifugation at 16,000 and 100,000 rcf was performed in an Optima XE-90 Ultracentrifuge with SW40 Ti rotor, open-top thin-wall polypropylene tubes (14 × 95 mm^2) (Beckman Coulter) and deceleration set to 4. Depending on the following experimental uses, larger and smaller EVs were kept separated or pooled, and pellets were resuspended in variable amounts of PBS or other reagents, as indicated in the respective methods or figure legends.

2.12 | Flow Cytometry of EVs

For surface staining of EVs, 1 µL of antibody (listed in Table 1) was diluted in 50-µL EV PBS and added to 50 µL of EV samples and incubated for 1 h at RT in the dark. For staining with Annexin V, EVs were diluted in 0.2 µm of filtered Annexin V binding buffer (Biolegend, San Diego, USA).

For intravesicular staining of cleaved CASPASE-3 (cCASP-3), EVs were permeabilised in 0.1% perm/wash buffer (BD Bioscience) for 40 min at RT in the dark. Antibody of 50 µL diluted in 0.1% BD perm/wash were added and incubated for 1.5 h at RT protected from light. After incubation, 200 µL of the according buffer was added to each sample, and samples were divided into two FACS tubes each. One of the two samples was measured directly at the Aurora (Cytek) flow cytometer, with the settings described above, whereas the other one was incubated with 0.1% Triton-x100 as a detergent control and measured after 30 min of incubation. Cytometer settings were adjusted for the acquisition of EVs using the Megamix-Plus SSC beads (Biocytex).

2.13 | miRNA Sequencing

For the isolation of miRNA from EVs, EV pellets were stored in QIAzol at −20°C, and miRNA was isolated using the miRNeasy mini Kit (Qiagen), following the manufacturer's instructions. Samples underwent small RNA sequencing, performed at BGI (BGI Tech Solutions, Hongkong). The bioinformatics analysis was conducted using CLC genomics workbench version 24 (Qiagen, Aarhus). Clean reads were imported, and miRNAs were quantified, CLC parameters (miRNA-Quantification) miRBase: miRBase-Release_v22/Prioritised species = *Schistosoma mansoni* or Mus musculus/Allow length-based isomiRs = Yes/Additional upstream bases = 2/Maximum mismatches = 2/Strand specific = Yes/Minimum sequence length = 18/Maximum sequence length = 25. Differential expression analysis was performed, and *P* values were adjusted using FDR 10%.

2.14 | Proteomics

2.14.1 | Sample Preparation

Samples (a pool of large and small T-EVs) were dissolved in 100-mM triethyl ammonium bicarbonate (TEAB) and 1% w/v sodium deoxycholate (SDC) buffer, boiled at 95°C for 5 min and sonicated with a probe sonicator. The samples were then pipetted into a 96-well LoBind plate (Eppendorf, Hamburg, Germany) placed on an Andrew+ Pipetting Robot (Waters, Milford, USA), which was used to execute all following steps. Reduction of disulfide bonds was achieved by incubating the samples using 10-mM dithiothreitol for 30 min at 56°C while shaking at 800 rpm. Afterwards, reduced disulfide bonds were alkylated in the presence of 20-mM iodoacetamide for 30 min at 37°C while shaking at 800 rpm. Then, carboxylate-modified magnetic E3 and E7 speed beads (Cytiva Sera-Mag, Marlborough, USA) at 1:1 ratio in LC-MS grade water were added in a 10:1 (beads/protein) ratio to each sample, following the single-pot, solid-phase enhanced sample preparation (SP3)-protocol workflow (Tyanova, et al. 2016). To bind the proteins to the beads, acetonitrile (ACN) concentration was raised to 50%. Subsequently, samples were shaken at 600 rpm for 18 min at RT. Magnetic beads were magnetised, and the supernatant was removed. Magnetic beads were further washed 2 times with 80% ethanol (EtOH) and then 2 times with 100% ACN. For tryptic digestion, the beads were resuspended in 100-mM AmBiCa and 250-ng trypsin (sequencing grade, Promega) was added before incubation at 37°C overnight with shaking at 500 rpm. The next day, trifluoroacetic acid (TFA) was added to a final concentration of 1% to inactivate trypsin. The samples were then shaken at 500 rpm for 5 min at RT. Finally, beads were magnetised, and the supernatant containing tryptic peptides was transferred into a new 96-well LoBind plate, ready for subsequent LC-MS/MS analysis.

2.14.2 | LC-MS/MS Measurements

Chromatographic separation of peptides was achieved with a two-buffer system (buffer A: H2O with 0.1% FA, buffer B: 80/20 (v/v) ACN/H2O with 0.1% FA) on a UHPLC (VanquishTM neo UHPLC system, Thermo Fisher). Attached to the UHPLC was a peptide trap (100 µm × 20 mm, 100 Å pore size, 5-µm particle size, C18, Thermo Fisher) or a PepMap Neo trap cartridge (300 µm × 5 mm, 100 Å pore size, 5-µm particle size, C18, Thermo Fisher) for online desalting and purification, followed by a 25-cm C18 reversed-phase column (75 µm × 250 mm, 130 Å pore size, 1.7-µm particle size, peptide BEH C18, nanoEase, Waters) or a C18 reversed-phase column (75 µm × 250 mm, 130 Å pore size, 1.7-µm particle size, peptide BEH C18, nanoEase, Waters). Peptides were separated using a 60- or 80-min method with linearly increasing concentration of buffer B from 2.5% to 37.5% over 50 or 70 min, respectively.

MS/MS measurements were performed on a quadrupole-orbitrap hybrid mass spectrometer (Exploris 480, Thermo Fisher Scientific). Eluting peptides were ionised using a nano-electrospray ionisation source (nano-ESI) with a spray voltage of 1,800 V and analysed in data-dependent acquisition (DDA) mode. For each MS1 scan, ions were accumulated for a maximum of 25 ms or until a charge density of 3×10^6 ions (AGC Target) was reached. Fourier transformation-based mass analysis of the data from the orbitrap mass analyser was performed covering a mass range of m/z 350–1400 with a resolution of 60,000 at m/z 200. Peptides being responsible for the 20 highest signal intensities per precursor scan with an intensity threshold of 8×10^3 and charge state from +2 to +6 were isolated within an isolation window of m/z 2 and fragmented with a normalised collision energy of 30% using higher energy collisional dissociation (HCD). MS2 scanning was performed, covering a mass range starting at m/z 120 and accumulated for 50 ms or to an AGC target of 1×105 at a resolution of 15,000 at m/z 200. Already fragmented peptides were excluded for 30 s.

2.14.3 | Data Analysis

LC-MS/MS data were searched with the Sequest algorithm integrated into the Proteome Discoverer software (v3.1.0.638, Thermo Fisher Scientific) against a reviewed murine Swissprot database, obtained in November 2023, containing 17,163 entries. Carbamidomethylation was set as a fixed modification for cysteine residues. The oxidation of methionine, pyro-glutamate formation at glutamine residues at the peptide N-terminus, as well as the acetylation and methionine loss of the protein N-terminus were allowed as variable modifications. The maximum number of missing tryptic cleavages was set at 2. Peptides between 6 and 144 amino acids were considered. A strict cutoff (FDR < 0.01) was set for peptide and protein identification. Quantification was performed using the Minora algorithm, implemented in the Proteome Discoverer.

2.14.4 | Statistical Analysis for Proteomics

Prior to the integration of two measurement batches, log2 transformation and column median normalisation were conducted across columns. Batch effects were removed using the BERT R package (v1.0.0) (Schumann et al. 2025) employing the reference method using the phenotype as a reference. Unpaired Student's *t*-test using a permutation-based FDR correction was conducted in the Perseus software (v.2.0.10.0) (Tyanova et al. 2016). Volcano plots to visualise the *t*-test results were generated using the ggplot2 package (v3.5.1). Genes from murine Hallmark gene sets for apoptosis and inflammatory response were annotated; gene sets were obtained from the Molecular Signature Database (Castanza et al. 2023; Subramanian et al. 2005). Gene set enrichment analysis was conducted using the fgsea R package (v1.30.0) (Korotkevich et al. 2016) against the gene ontology (GO)—molecular function database after ranking the proteins according to their foldchange.

2.15 | *S. mansoni* Egg Count

A piece of the left loop of the liver was weighed and incubated in 2% KOH for 8 h at 37°C in a 24-well plate with a grid. The tissue was dissolved by pipetting up and down, and the parasitic eggs were counted on a bright field microscope using 4× magnification. Eggs per gram/liver were then calculated.

2.16 | *S. mansoni* Infection

S. mansoni cercariae preparation was obtained from *helmin*Guard (https://helminguard.de/). Briefly, to obtain single-sex cercariae, *Biomphalaria glabrata snails* (Brazilian strain) were individually exposed to one *S. mansoni* miracidium each. Upon patency (5 weeks after infection), the sex of the cercariae released from individual snails was determined by polymerase chain reaction (PCR). Separately, male and female cercariae-shedding snails were transferred to petri dishes containing conditioned water and exposed to light for 2–4 h. Cercariae were passed through 50- and 20-μm filters, rinsed with re-mineralised distilled water, and recovered by flushing the 20-μm filter backwards.

Next, 10-μL of cercariae solution was diluted with 100-μL distilled water, cercariae were then immobilised using 1-mL Lugol solution and counted under a light microscope in a 48-well plate with a grid. About 20–35 *S. mansoni* cercariae (1:1.2 male-to-female ratio) were further diluted with PBS up to a volume of 200 μL and injected s.c. in 8- to 12-week-old C57BL/6 mice. Mice were sacrificed at week 8 post-infection, and the liver and blood were collected for downstream analysis.

2.17 | EV Injection in *S. mansoni*-Infected Mice

LiveT-EVs and aT-EVs were isolated as described above. A total of 5×10^9 EVs (a pool of small and large EVs) diluited in 200-μL EV PBS were injected i.v. in the lateral tail vein of *S. mansoni*-infected mice at weeks 6 and 7 post-infection (p.i.). Control mice were injected with 200 μL of 0.2-μm filtered PBS. Mice were sacrificed at week 8 p.i., and the liver and blood were collected for downstream analysis.

2.18 | Histology

Liver tissue was fixed in 37% formalin for 24 h, followed by storage in PBS at RT. Samples were processed, embedded, sectioned, and stained with haematoxylin and eosin (H&E) at the Core Facility Mouse Pathology (University Medical Center Hamburg Eppendorf) following routine methods. The histopathological scores were assigned by a pathologist blinded to the experimental manipulation. Histological grading and staging of chronic hepatitis were assessed using the modified Histological Activity Index (mHAI /Ishak score). This system evaluates necroinflammatory activity and fibrosis in liver biopsy samples. The grading component includes periportal or periseptal interface hepatitis (piecemeal necrosis, 0–4 points), confluent necrosis (0–6 points), focal lytic necrosis/apoptosis (0–4 points) and portal inflammation (0–4 points). High scores indicate the severity of the respective feature, resulting in an overall scoring from 0 to 18 points, which reflects the inflammatory activity. Scores were assigned semi-quantitatively by trained pathologists to ensure consistency. The mHAI was selected for its reproducibility and clinical relevance in monitoring disease progression and evaluating therapeutic responses (Ishak et al. 1995).

2.19 | ALT Levels

Blood from *S. mansoni*-infected mice was collected in tubes containing 20-μL heparin, centrifuged and the serum stored at −20°C. The Reflotron (Roche, Basel, Switzerland) was used to measure the levels of alanine aminotransaminase (ALT) in the serum. Briefly, 32 μL of serum per mouse was added to a Reflotron GPT (ALT) test stripe. Measurements were performed at 25°C.

2.20 | Cell Culture

Cell lines WEHI-164 (fibroblast-like cell) and Hepa-1-6 (hepatoma cell) were kindly provided by collaborators at the BNITM, Hamburg. Cell lines and primary cells were cultured at 37°C and 5% CO_2. All cell cultures and in vitro functional experiments were performed under sterile conditions.

2.21 | Generation of BMDMs

Bone marrow was isolated from the mouse femur and tibia by cutting one end of each bone and placing the bones, with the open end facing downard, into a 0.5-mL tube with a pinched hole, which was inserted into a 1.5-mL tube. Bone marrow cells were recovered by centrifugation at 16,000 rcf for 2 min. The hematopoietic pluripotent stem cell homogenate was filtered over a 40-μm strainer, and cells were plated in 10-mL RPMI (PAN-Biotech) containing 20% FCS (Capricorn Scientific), 15%–30% L929 supplement, and 0.5% Gentamycin (Capricorn Scientific) in a 10-cm petri dish. BMDMs were differentiated over a time course of seven days at 37°C and 5% CO_2. On day 3, half the media was replaced with fresh media. On day 5, the cells were split. On day 7, differentiated BMDMs were detached, counted, and if not stated otherwise, 0.33×10^6 cells per well were seeded into a 24-well plate in a 500–1000-μL medium to perform in vitro experiments.

2.22 | CFSE Labelling of EVs

EVs were labelled using Vybrant CFDA SE Cell Tracer Kit (ThermoFisher Scientific). CFDA SE is non-fluorescent until it is converted to CFSE by esterase enzymes. The manufacturer's instructions were optimised for application in EV research as follows: 0.33-μL CFDA SE (10 mM) was diluted in 1000 μL of 0.2-μm filtered PBS, added to 1 mL of EV suspension and incubated at 37°C in the dark for 2 h. 10 mL of EV depleted medium was added, and large and small EVs were pelleted at 16,000 or 100,000 rcf, respectively.

2.23 | in vitro Assays

Unless stated otherwise, cells were counted and seeded into wells of a 24-well plate at a concentration of 0.33 × 106 cells/well in 500 μL of appropriate medium and incubated at 37°C/5% CO_2 for the indicated lengths of time, before being processed for further analyses. EVs and/or cytokines were added in concentrations as indicated in the individual experiments. To block the uptake of

EVs, BMDMs were treated with Cytochalasin D (10 μg/mL) for 1 h before incubation in the presence of EVs (a pool of small and large EVs). Cells were then washed 3× with PBS before being harvested using cold PBS(on ice), or directly using buffer RTL (Qiagen), depending on the following experiments.

2.24 | Fibroblast Migration Assay

WEHI-164 cells were seeded as 0.2×10^6 cells per well into a 24-well plate in 1000-μL RPMI containing 10% FCS and 0.5% Gentamycin. When cells were settled, two scratches were made using a 200-μL pipette tip (Sarstedt) disrupting the fibroblast monolayer from left to right in the upper and lower half of each well. The wells were gently washed 3 times with PBS and then, 20-μg EVs (protein concentration; a pool of small and large EVs) were added in 200 mL of fresh media. Each well was photographed using the EVOS FL Auto Imaging system (ThermoFisher Scientific), all photographed positions were saved and photographed again after 24-h incubation at 37°C and 5% CO_2. The gap closure was measured using ImageJ. The diameter of the scratch separating the fibroblasts was measured in the pictures taken at 0 and 24 h at 3 positions. The average diameter for each time point was calculated, and the percentage of gap closure after 24 h in relation to 0 h was calculated.

2.25 | Bulk-RNA Sequencing

RNA isolated from BMDMs treated with liveT-EVs or aT-EVs for 24 h underwent RNA sequencing, performed at BGI (BGI TECH SOLUTIONS, Hongkong). Library preparation and transcriptome sequencing were performed using 100 bases/paired-end reads on the BGI's DNBSEQ Technology Platform. The mRNA sequencing with subsequent filtering (removal of adapters, low-quality reads, N reads and polyX) and quality control was performed on DNBSEQ Technology by BGI. The reads for each sample were aligned to the mouse genome (GRCm39) using the STAR aligner (version 2.7.10b). Obtained count matrices were analysed as follows: Guided by visual inspection of the count distributions, genes were required to have log10-transformed raw counts greater than 1.5 in a minimum of three samples to be retained for downstream analysis. Calculation of the fold change of each gene between liveT- and aT-EVs was performed using DESeq2 (version 1.40.2). The top 15 genes with the highest log2FC and 15 genes with the lowest log2FC were defined as the top differentially expressed (DE) genes. The row-scaled values of these genes were sorted by hierarchical clustering and plotted using the pheatmap package (version 1.0.12). To identify targetable processes and pathways, all DE genes with log2FC > 0.5 as upregulated in liveT-EVs and log2FC < -0.5 as upregulated in aT-EVs were grouped. These gene sets were used to perform an overrepresentation analysis using the enrich KEGG method from the clusterProfiler package (version 4.8.3). The gene symbols were converted to Entrez IDs by org.Mm.es.db (version 3.17.0). The parents of each term were queried using KEGGREST (version 1.40.1). Further, GO terms 'Biological Process 2023' were calculated with the enrichR package (version 3.4).

2.26 | RNA Isolation

A piece of the right renal fossa loop of the liver was stored in RNAprotect Tissue Reagent (Qiagen, Hilden, Germany). For RNA isolation, part of the tissue was transferred into 200 μL of TRIzol. The tissue was disrupted using a tissue homogeniser (KIMBLE PELLET PESTLE) and 800 μL of TRIzol were added. RNA was isolated from the lysed samples using phenol–chloroform extraction. The final RNA pellet was air-dried and dissolved in 150 μL of RNase-free water.

For the isolation of mRNA from BMDMs for sequencing, cells were lysed using the QIAshredder column (Qiagen), and mRNA was isolated using the RNeasy mini Kit (Qiagen), following the manufacturer's instructions.

The mRNA concentration and purity were measured via Nanodrop2000 (ThermoFisher Scientific). The mRNA samples were stored at −80°C until further processing.

2.27 | RT-qPCR

Reverse transcription of RNA was performed using the iScript cDNA synthesis Kit (BioRad) according to the manufacturer's instructions. RT-qPCR was performed using the Maxima SYBR Green qPCR Master Mix (Thermo Fisher) on a Corbett Rotor-Gene (Corbett research/Qiagen). All reactions were performed in duplicates, with *Gapdh* as a reference gene. Data were analysed using the RotorGene 6000 Series Software, followed by the ddCT method. The primers were purchased from Eurofins (Table 3).

2.28 | Chemiluminescence Assay

Intracellular and extracellular ROS production was measured via a chemiluminescence assay. Briefly, 0.33×10^6 BMDMs were plated in a 96-well plate in 150 μL of appropriate medium and incubated at 37°C/5% CO_2 for 2 h. 20 μg of EVs (protein concentration; a pool of small and large EVs) and/or 10 μg/mL of LPS were added to the respective wells. After 24 h of incubation of the BMDMs in the presence of EVs, the media was removed, cells were washed 3 times with HBSS containing 0.5% FCS and 148 μL of HBSS containing 0.5% FCS were added to each well. The luminol master mix consisted of 5 μL of luminol (100 mM), 45 μL of borate buffer (0.2 M H_3BO_3, 0,2 M Na_2B4O_7 x 10 H_2O), 10 μL of horse radish peroxidase (500 U/mL, Merck), 2.4 μL of Catalase (100 mg/mL in potassium phosphate buffer, Sigma) and 2 μL of SOD (1 mg/mL, Sigma), per well. According to the conditions, 24 μL of PMA (0.5 μM, Cayman) or PBS per well were added. The chemiluminescence was measured every 2 min for 2 h at the Tecan Spark microplate reader (Tecan Life Sciences) at 37°C.

2.29 | Statistics

Statistical analyses were performed using Prism 10 (GraphPad). Detailed information is provided in the figure legends. Briefly, outliers were removed using the ROUT method, and data were

TABLE 3 | List of primers.

Gene	Sequence (5′ → 3′)
mGapdh	Fwd: TCCCACTCTTCCACCTTCGA Rev: AGTTGGGATAGGGCCTCTCTT
mNos2	Fwd: ACCCACATCTGGCAGAATGAG Rev: AGCCATGACCTTTCGCATTAG
mSerpinb2	Fwd: ACCCAGAGAACTTCAGTGGCTG Rev: GAGAGAGGAGAAGGCTGAATGG
mSocs2	Fwd: GGTTGCCGGAGGAACAGTC Rev: GAGCCTCTTTTAATTTCTCTTTGGC
mSocs5	Fwd: GACGGCTTAGTATCGAAGAA Rev: GCTTATACAATGGGTTGACC

tested for normality prior to statistical testing. The Mann–Whitney *U* test was used when only two groups within one single graph were compared (without interest in their relation to other samples). The Wilcoxon test was used for comparison between two paired conditions. The Kruskal–Wallis test followed by Dunn's multiple comparison was used when comparing multiple conditions within one graph. Normally distributed data were analysed using an unpaired *t* test. The p value ≤ 0.05 was considered statistically significant (*$p \leq 0.05$, **$p < 0.01$, ***$p < 0.001$, ****$p < 0.0001$). Data points without specific labels or labelled 'ns' indicate non-statistically significant results. Data are shown as mean ± SEM. Unless otherwise stated in the figure legend, each data point represents one independent biological replicate.

3 | Results

3.1 | EVs Isolated From the Livers of *S. mansoni*-Infected Mice Are Enriched in Vesicles Originating From Dying Immune Cells

During *S. mansoni* infection, the liver is the focal point of damage. Parasite eggs trapped in liver tissue cause the infiltration and activation of various immune cells, resulting in granuloma formation around the egg (Schwartz and Fallon 2018). Immune cell activation is associated with the active release of soluble mediators and various cellular components, such as EVs (Robbins and Morelli 2014; Wahlgren et al. 2012). To determine the features of EVs released in the liver of infected mice, hepatic EVs were isolated by differential centrifugation, and the EVs obtained in the 100,000 rcf pellet were characterised for their size, morphology and surface marker composition.

EVs isolated from the liver of naïve or 8-week *S. mansoni*-infected mice were analysed via Transmission Electron Microscopy (TEM) and differences in morphology size and concentration were observed (Figure 1A; Figure S1). Nanoparticle tracking analysis (NTA) was performed to quantify the size and concentration distribution of the particles in the 100,000 rcf pellet. Both naïve and infected liver-derived EVs range in size between 50 and 700 nm in diameter, with the highest concentration of EVs at 222 and 218 nm, respectively (Figure 1B). We detected a 10-fold increase in the concentration of EVs isolated from infected livers compared to the naïve controls (Figure 1B). Even though the proportions of large EVs (>200 nm) and small EVs (<200 nm) detected in the 100,000 rcf pellet via NTA are similar in naïve and infected mice (Figure 1C), the amount of large EVs per liver is significantly higher in infected liver-EVs compared to the naïve counterpart, as based on calculation from NTA data (Figure 1D). We however cannot exclude that higher liver-to-body weight ratio and increased numbers of hepatic cells in infected mice (Dannenhaus et al. 2024) contribute to the increase in EV concentration detected.

We did not detect contamination of liver-derived EVs with cell components, as shown by the western blot analysis of the expression of the Golgi protein GM130 in the EVs compared with primary thymic lymphocytes, here referred to as thymocytes, either live (liveT) or apoptotic (aT) (Figure 1E). In contrast, the cytosol marker TSG101 was detected in both the cells and the liver-derived EVs.

To further characterise differences between naïve and infected liver-derived EVs, their surface epitope composition was analysed via MACSPlex, and additionally selected markers confirmed via flow cytometry (Figure 1F). Herein, naïve liver-derived EVs showed overall lower abundance and expression of all markers than infected liver-derived EVs, with MHC-II being the highest expressed surface epitope on both EV samples. Enrichment of immune cell-associated markers on infected liver-derived EVs, such as CD45, CD11b, CD9, MHC-II, and CD11c, suggests that during *S. mansoni* infection, liver EVs are partially originating from immune cells (Figure 1F).

To further define the features of cells accumulating in the infected liver, we first quantified the amount of $CD45^+$ leukocytes. As previously described, and in line with the infiltration of immune cells being a key feature of the immune response against *S. mansoni* infection, we detected higher numbers of $CD45^+$ cells in the livers of infected than in naïve mice (Figure 1G). Given the role of dying cells on shaping the inflammatory response and the consequent infection outcome, we next determined the cell counts and cellular identity of the dying cells by assessing surface Phosphatidylserine (PtdSer) expression, via Annexin V staining, on different $CD45^+$ hepatic leukocyte populations. We observed an increased amount of Annexin V^+ B cells ($B220^+$), T cells ($CD3^+$ and $CD4^+$ or $CD4^-$), neutrophils ($Ly6G^+$), dendritic

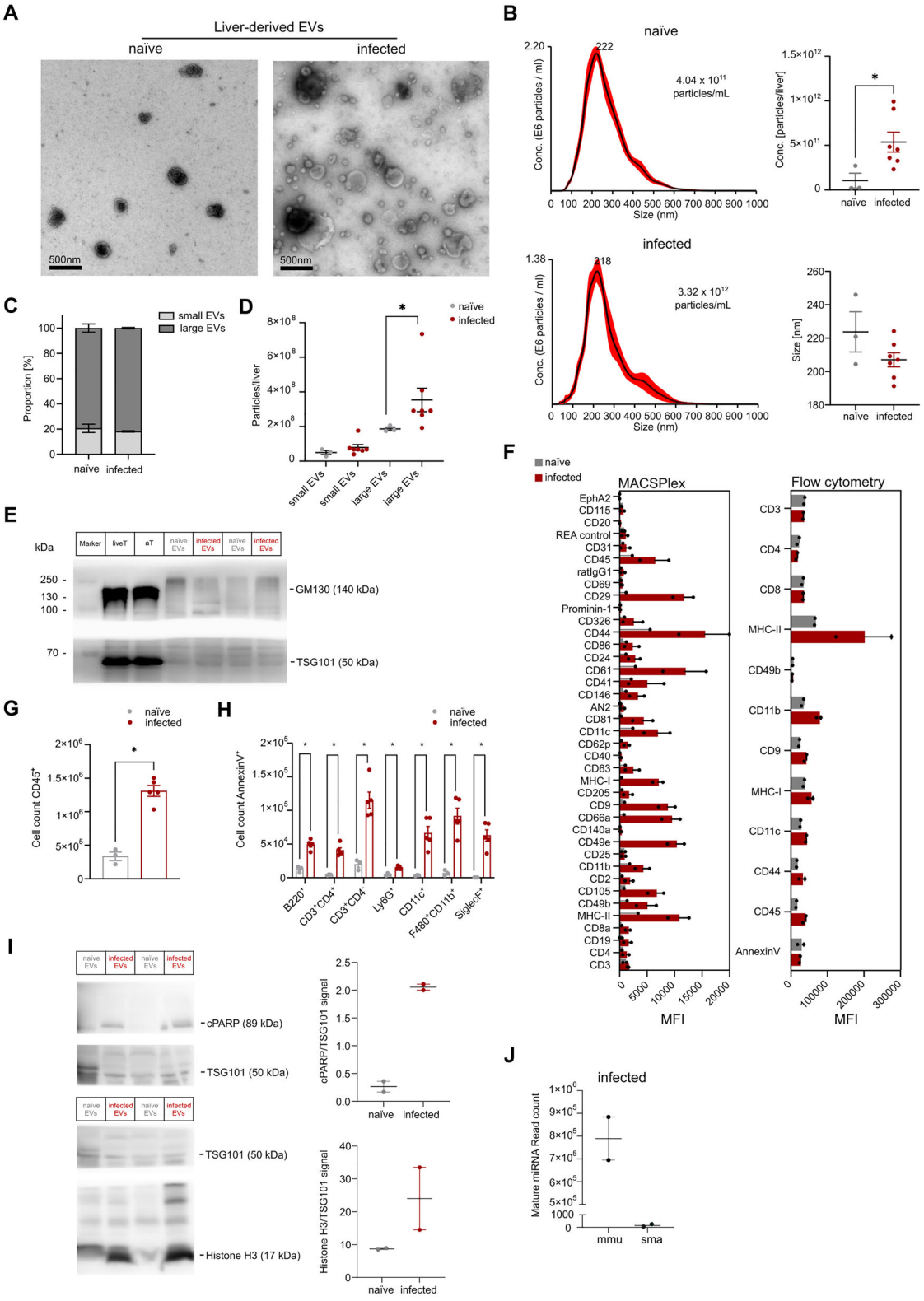

FIGURE 1 | Extracellular vesicles accumulate in the liver of *S. mansoni*-infected mice. (A) Representative TEM images of EVs isolated from the liver of one representative naïve and one representative *S. mansoni*-infected mouse. (B) NTA of liver-derived EVs measured using the Nanosight LM14C. Representative histograms (left) showing the average size and concentration of liver-derived EVs isolated from one representative naïve and one representative *S. mansoni*-infected mouse. Numbers indicate the mode size; red line indicates means ± SEMs. Pooled quantification (right) of particles per liver analysed (top) and the corresponding mode size (bottom) are shown below. $n = 3 - 7$; Mean ± SEM. Mann–Whitney U test, $^*p \leq 0.05$. (C) Proportion of small EVs (<200 nm) and large EVs (>200 nm) in naïve ($n = 3$) and infected liver-derived EVs ($n = 7$), as quantified via NTA from the 100,000 rcf pellet. (D) Count of small and large particles per liver in the 100,000 rcf pellet in naïve and infected liver-derived EVs. $n = 3–7$; Mean ± SEM. Mann–Whitney U test, $^*p \leq 0.05$. (E) Western blot analysis of GM130 and TSG101 expression in naïve and infected liver-derived EVs, with live

(liveT) and apoptotic thymocytes (aT) used as controls. (F) Surface epitope detection of liver-derived EVs from naïve (grey) or *S. mansoni*-infected mice (red) using MACSPlex (left) and flow cytometry (right). Data from two independent experiments are shown; each data point represents a pool of EVs isolated from 6 – 9 livers. Data are plotted as mean ± SEM. (G) $CD45^+$ cell count in the liver of naïve (grey) vs. *S. mansoni*-infected (red) mice. $n = 5–8$; mean ± SEM. Mann–Whitney U test, $*p \leq 0.05$. (H) Counts of Annexin V^+ cells within different leukocyte populations isolated from the livers of naïve vs. *S. mansoni*-infected mice. $n = 5 – 8$; Mean ± SEM. Multiple unpaired T tests, $*p \leq 0.05$. (I) Western blot analysis of cPARP and Histone H3 expression in naïve and infected liver-derived EVs, and the corresponding bar graphs reporting the ratio to TSG101 signal intensity as analysed via ImageJ. $n =$ 2/condition (6 - 9 livers pooled); Mean ± SEM. (J) Bar graph reporting the read count of mature miRNA detected in EVs from *S. mansoni*-infected livers, classified as either murine miRNAs (mmu) or *S. mansoni* miRNAs (sma). $n = 2$/condition (6 - 9 livers pooled); Mean ± SEM.

cells ($CD11c^+$), macrophages ($F4/80^+CD11b^+$) and eosinophils ($SiglecF^+$) (Figure 1H; Figure S2) in the infected livers compared to the naïve controls. In line, liver EVs derived from *S. mansoni*-infected mice show enrichment of the ApoEV markers Histone H3 and cleaved PARP (cPARP) compared with those from naïve mice confirming that EVs isolated from infected livers are enriched in vesicles originating from dying cells (Figure 1I).

To assess the relative enrichment of mouse- versus *Schistosoma*-specific EVs, we performed miRNA sequencing of EVs isolated from the livers of infected mice. Among the detected miRNAs, we obtained an average of 789,690.5 reads specific to mouse miRNAs (mmu) and 159 reads specific to *S.mansoni* miRNAs (sma) (Figure 1J), indicating that host-derived miRNAs accounted for the vast majority of miRNAs in infected liver EV preparations.

Altogether, these data indicate that EVs released in livers of *S. mansoni*-infected mice originate from a diverse range of both live and dying host immune cells. Although we cannot exclude the occurrence of different forms of cell death in the infected mice, our data suggest that Annexin V^+ cells accumulate in the liver compared to naïve controls and represent one of the sources of EVs within the infected host.

3.2 | The Properties of Released EVs Are Determined by the Cell of Origin's Fitness Status

T-cell apoptosis has been identified as a crucial factor in the Th1/Th2 immune response switch that occurs during the course of schistosomiasis (Estaquier et al. 1997). Additionally, we have recently shown that the engulfment of apoptotic neutrophils and T cells by Mφs in the infected liver is essential for promoting parasite egg clearance during the chronic phase of schistosomiasis (Liebold et al. 2024). Therefore, based on the key role of dying T cells in schistosomiasis progression, we chose to isolate EVs from the supernatants of either live or apoptotic thymocytes, as a model to study the distinct effects of EVs released from live versus $PtdSer^+$ dying T cells. Hereby, EVs from live thymocytes (liveT-EVs) were isolated after 2–3 h of thymocyte culture in vitro, whereas EVs from dying/apoptotic thymocytes (aT-EVs) were isolated after 24 h of culture in media containing low amounts of serum (5% FCS). Annexin V and propidium iodide (PI) staining was performed to evaluate apoptosis induction (Figure S3). The thymocytes supernatant was used for isolating small or large EVs via centrifugation. We observed that aT generally release more EVs that are larger in size, as defined via TEM and NTA (Figure 2A, B). Additionally, EVs derived from live and apoptotic thymocytes show similar surface epitope compositions, with MHC-II detected on both EV samples, similar to what is observed in liver-derived EVs isolated from infected mice. Additionally, we detected enrichment in the T cell markers CD4 and CD8 in aT-EVs compared to liveT-EVs (Figure 2C). Both EV samples show similar levels of PtdSer, as detected via Annexin V staining, regardless of the origin or size of the EV samples (Figure 2D; Figure S4). This suggests that, in our experimental setting, PtdSer can be more accurately defined as a bona fide marker for EVs, essential for EV biogenesis as previously described (Frey and Gaipl 2011), rather than a marker reflecting the fitness/activation status of the cell of origin.

Next, we aimed to detect a marker that identifies explicitly ApoEVs. Therefore, we stained the EV fractions intravesicularly for cleaved CASPASE-3 (cCASP-3). Notably, small EVs released by aTs contain more cCASP-3 than liveT-EVs (Figure 2E; Figure S5), indicating that cCASP-3 serves as a marker of the fitness status of the EVs' cell of origin under our experimental conditions. The abundance of cCASP-3 in aT-EVs, but not liveT-EVs, was also confirmed via western blot (Figure 2F).

To further dissect the features of liveT- and aT-EVs, we analysed their protein content via mass spectrometry. The protein cargo composition differs significantly between liveT- and aT-EVs (Figure 2G). In particular, we observed expression of proteins, such as HMGB2, PDCD4 and RELA (Figure 2H), which are annotated as involved in inflammatory response and apoptosis via Molecular Signature Database, as well as proteins involved in pathways associated with EV biogenesis (Figure S6).

3.3 | EVs Derived From Live and Apoptotic Cells Differentially Impact Hepatocyte Damage During *S. mansoni* Infection

Given the distinct features of EVS originating from liveT or aT, we next aimed to study their effects in an in vivo pathological setting, where the accumulation of dying cells and the resulting immune response have been described as key factors influencing disease pathogenesis (Estaquier et al. 1997; Knuhr et al. 2018). During *S. mansoni* infection, the balance between an initial type 1 pro-inflammatory response and the subsequent type 2-mediated tissue remodelling response drives the outcome of the infection. This transition, characterised by reduced IFN-γ production and increased IL-4 and IL-13 secretion by basophils (Knuhr et al. 2018; Silveira et al. 2004), is triggered by the release of eggs by the mature parasite. This shift, while providing protection against excessive liver damage, also facilitates the establishment of chronic infection (Molehin 2020). In this scenario, the magnitude of CD4 T cell-mediated immunopathology has been described to correlate inversely with the extent of CD4 T cell apoptosis

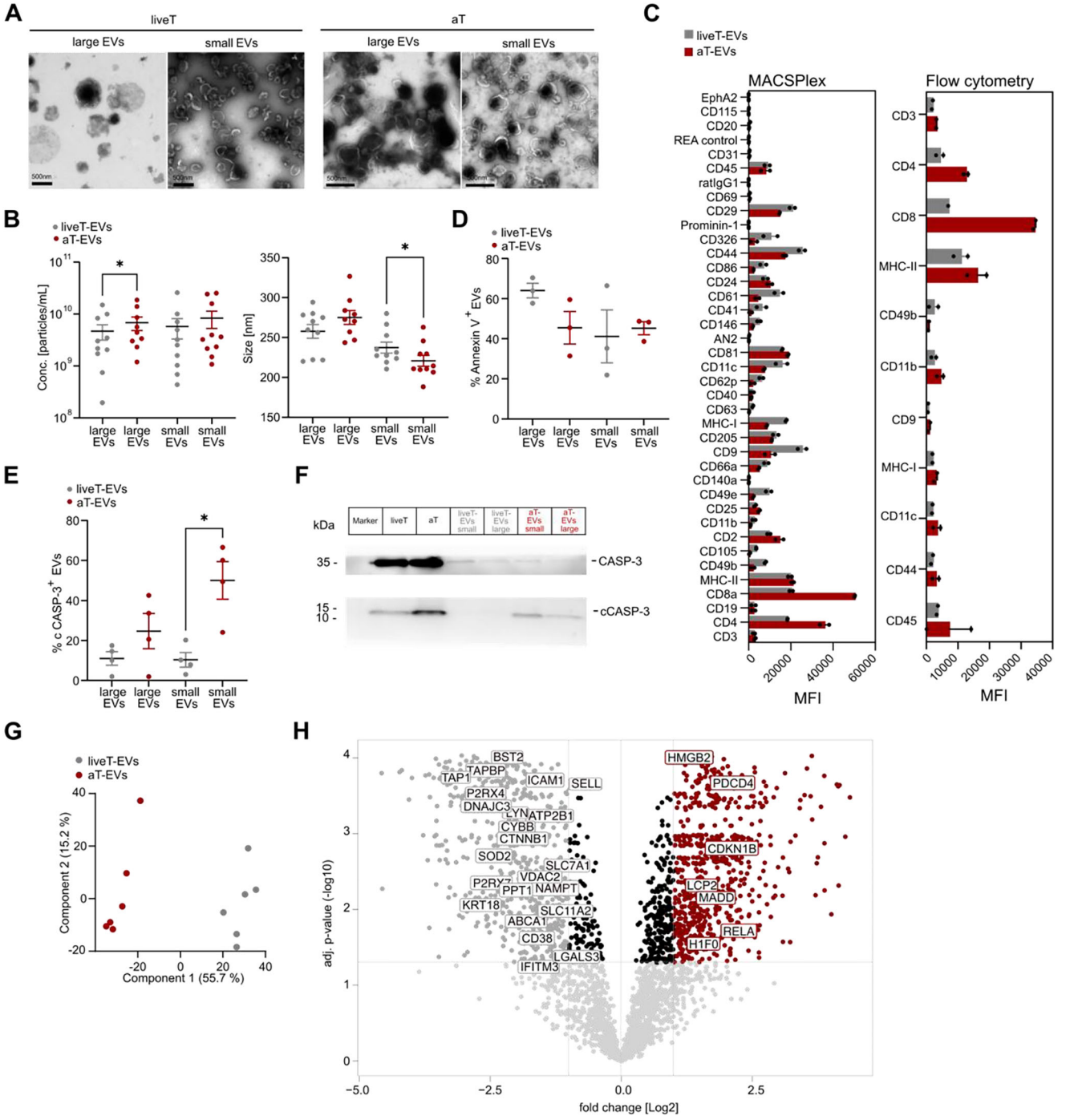

FIGURE 2 | Extracellular vesicles with distinct features derive from living and dying cells. (A) Representative TEM images of fractions enriched in small and large EVs isolated from live (liveT) and apoptotic thymocytes (aT). (B) Quantification of particle concentration (left) and mode size (right) as measured from the small and large EV fractions isolated from liveT (grey) and aT (red), as measured by NTA. $n = 10$; Mean ± SEM. Wilcoxon test, $*p \leq 0.05$. (C) Expression of surface markers in liveT-EVs and aT-EVs (a pool of large and small EVs), as detected by MACSPlex (left) and flow cytometry (right). Data from 2 – 3 independent experiments are reported. Mean ± SEM. Multiple Mann–Whitney tests. (D) Expression of Annexin V in liveT- (grey) and aT-EVs (red), as detected by flow cytometry. $n = 3$; Mean ± SEM. Mann–Whitney test. (E) Expression of intravesicular cleaved CASPASE-3 (cCASP-3) in liveT- (grey) and aT-EVs (red), as detected by flow cytometry. $n = 4$; mean ± SEM. Mann–Whitney test, $*p \leq 0.05$. (F) Western blot analysis of total CASP-3 and cCASP-3 expression in large and small liveT-EVs or aT-EVs, with liveT and aT used as controls. (G) PCA plot showing the clustering of liveT- and aT-EVs (a pool of large and small EVs) based on proteomic profiles measured by mass spectrometry. (H) Volcano plot reporting proteins differentially expressed in liveT- (grey) vs. aT-EVs (red) as resulted from proteomic analysis. Proteins involved in Hallmark pathways *Apoptosis* and *Inflammatory Response*, according to Gene set enrichment analysis (GSEA), are indicated.

(Rutitzky et al. 2003). Given this, we next assessed whether the injection of aT-EVs into *S. mansoni*-infected mice could affect disease progression. To this end, 5×10^9 liveT-EVs, aT-EVs or 200-µL PBS as vehicle control, were injected into wild-type mice at weeks 6 and 7 post-infection, when parasitic egg release is occurring.

Although the EV injection showed no impact on egg counts in the liver of infected mice compared to the PBS-treated controls (Figure 3A), as well as no changes in the overall architecture of the tissue, as shown by H&E staining (Figure 3B; Figure S7), ALT levels were significantly lower in mice receiving aT-EVs compared to PBS controls, indicating lower degrees of hepatocyte damage (Figure 3C). Of note, *S. mansoni* infection causes chronic hepatocyte damage over a prolonged time course; therefore, ALT levels are generally expected to be lower than in models of acute liver damage (Su 2019). Next, to evaluate whether the injection of EVs would impact Mφ profile, the phenotype of hepatic Mφs was analysed via flow cytometry. No significant changes could be detected in the expression of markers featuring alteration in tissue remodelling function, such as iNOS, ARG1 and YM1 (Figure 3D; Figure S8). To further assess the extent of liver damage, apoptosis-related proteins were quantified via western blot in the infected livers (Figure 3E–H). The ratio of cCASP-3 to total CASPASE-3 (CASP-3) was not significantly altered in mice that received aT-EVs or liveT-EVs compared to PBS controls (Figure 3E, F). Additionally, no difference in the expression of cPARP, a downstream target of cCASP-3 in the apoptosis signalling cascade, was observed (Figure 3G, H), indicating that no changes in the overall occurrence of apoptosis were detected. Overall, these data suggest that EVs derived from apoptotic versus live cells, despite their differential features (Figure 2), have a modest effect on the progression of *S. mansoni* infection, primarily through decrease in hepatocyte damage, as indicated by lower ALT levels.

3.4 | EVs From Live and Apoptotic T Cells Can Differentially Impact Immune and Non-immune Cell Function

Considering the distinct phenotypical and physical characteristics of EVs derived from dying versus living cells, as well as their impact on liver damage, we next investigated the effects of EV uptake on potential liver target cells. Therefore, we established an in vitro system to track EV uptake in different cell types, both of immune and non-immune origin. To this end, EVs were labelled with the fluorescent dye CFSE (Figure S9) and incubated with target cells, that is, hepatocytes, fibroblasts, and BMDMs, whose role in disease progression and fibrosis development has been extensively described in models of chronic infections such as schistosomiasis (An et al. 2020; David J. et al. 1978). Incubation of cells in the presence of EVs was performed for 24 h, and the uptake of EVs on the target cells was analysed by flow cytometry, by measuring the mean fluorescent intensity (MFI) of CFSE. Firstly, target cells were shown to efficiently uptake either liveT- or aT-EVs. Even though the same protein concentration of liveT- and aT-EVs were given to the target cells, BMDMs and fibroblasts showed a trend toward increased uptake of liveT-EVs compared to the corresponding apoptotic counterparts. On the contrary, hepatocytes preferentially uptake aT-EVs (Figure 4A–C). CFSE labelling is a useful tool allowing to distinguish cell populations that have taken up ($CFSE^+$) or not taken up ($CFSE^-$) EVs. When further gating these populations, $CFSE^+$ BMDMs and fibroblasts show a significant difference, whereas hepatocytes show a tendency, toward higher Ki67 expression. This suggests that, in vitro, the uptake of both liveT- and aT-EVs is associated with increased target cell proliferation (Figure 4A–C; centre panel; Figure S9 and S10). Next, to investigate whether cCASP-3 accumulating in aT-EVs was transferred to the target cells, as previously described (Böing et al. 2013), we analysed its abundance on BMDMs, hepatocytes and fibroblasts. No detectable differences in the percentage of cCASP-3 were observed in target cells when incubated in the presence of liveT- EVs or aT-EVs compared to the untreated controls (Figure 4A–C, right panel; Figure S11). Given the role of fibroblasts in orchestrating both the healing and the fibrotic process in the damaged liver (Kisseleva and Brenner 2021), and in light of our data showing that fibroblasts can take up EVs and this results in enhanced proliferative capacity, we next addressed the impact of EVs on fibroblast wound healing capacity. To this end, we performed an in vitro scratch assay and evaluated whether incubation in the presence of liveT- or aT-EVs affects the ability of fibroblasts to close a gap, mimicking wound healing. We observed that aT-EVs, but not liveT-EVs, enhanced fibroblast wound healing capacity, as measured by the percentage of gap closure after 24 h (Figure 4D), suggesting that aT-EVs directly influence fibroblast-mediated tissue remodelling activity.

3.5 | EVs From Dying Cells Trigger Nitric Oxide Production by Macrophages

Next, we set out to better characterise Mφs, which exhibit the capacity to sense vesicles associated with alteration in the environment (Tang et al. 2022). To dive deeper into the molecular changes induced in target Mφs by vesicles originating from cells with different fitness levels, we performed bulk RNA-Seq on BMDMs incubated in the presence of liveT-EVs or aT-EVs in vitro for 24 h. We identified a total of 11,125 differentially expressed (DE) genes between liveT- and aT-EV-treated BMDMs, and analyzed the 15 genes with the absolute highest log2 fold change (log2FC) in each condition (Figure 5A). Interestingly, *Nos2*, the gene encoding for the inducible nitric oxide synthase (iNOS), *Cish*, a member of the suppressor of cytokine signalling (SOCS) family and *Serpinb2*, encoding for the plasminogen activator inhibitor type-2, were among the genes whose expression was induced selectively by exposure of BMDMs to aT-EVs. Gene ontology (GO) term analysis of the most DE genes among the two conditions reveals that BMDMs treated with aT-EVs upregulate nitric oxide production pathways (Figure 5B). Further validation via RT-qPCR was performed (Figure 5C).

We next confirmed the higher expression of iNOS in BMDMs incubated in the presence of aT-EVs than the corresponding control counterpart (liveT-EVs) at the protein level (Figure 5D), as detected via flow cytometry. Higher iNOS expression is associated with increased production of nitric oxide, a reactive nitrogen species (RNS), as well as other reactive oxygen species (ROS), which, in turn can regulate iNOS function by shifting the balance of NO and superoxide production (Sun et al. 2010; Zhao et al. 2010). To define whether the increase in iNOS levels results in elevated intra- and extracellular ROS production, we stimulated

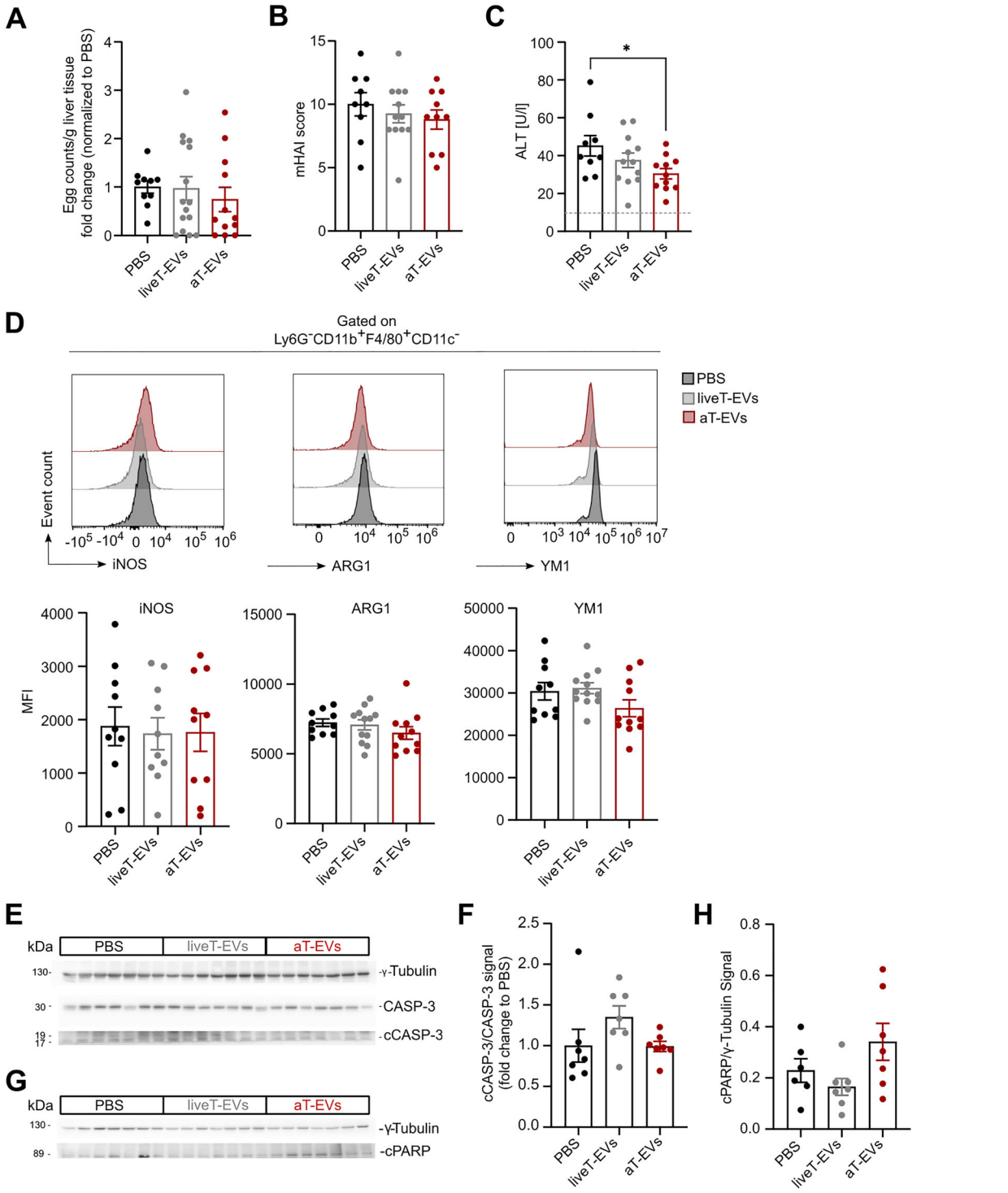

FIGURE 3 | EVs from live and apoptotic cells alter ALT levels during *S. mansoni* infection. EVs from live (liveT) or apoptotic thymocytes (aT) (a pool of small and large EVs), or PBS, as control, were injected to *S. mansoni*-infected mice, 6 and 7 weeks p.i. One week later (week 8 p.i.), liver and blood are collected. (A) Parasitic egg counts per g liver tissue of infected mice. Data are normalised to infected mice injected with PBS control. $n = 10–15$; mean ± SEM. Mann–Whitney U test. (B) Histological grading of liver damage according to the mHAI score from H&E-stained liver sections. $n = 6–11$; mean ± SEM. Mann–Whitney U test. (C) ALT levels measured in the serum. The dotted line represents the mean value of ALT levels in aged-matched naïve uninfected mice. $n = 9–12$; mean ± SEM. Mann–Whitney U test, $^*p \leq 0.05$. (D) Representative histograms and bar graphs reporting the median fluorescence intensity (MFI) of iNOS, ARG1 and YM1 expression in hepatic macrophages isolated from *S. mansoni*-infected mice after injection of liveT-, aT-EVs or PBS as control, as detected via flow cytometry. $n = 10–12$; mean ± SEM. Mann–Whitney U test. (E) Western blot analysis for the expression of cCASP-3 on total liver tissue. (F) Bar graph reporting the ratio of cCASP-3 to CASP-3 signal intensity as analysed via ImageJ. $n = 7$; mean ± SEM. Mann–Whitney U test. (G) Western blot analysis for the expression of cleaved PARP on total liver tissue. (H) Bar graph reporting the ratio of cPARP to γ-TUBULIN signal intensity as analysed via ImageJ. $n = 7$; mean ± SEM. Mann–Whitney U test.

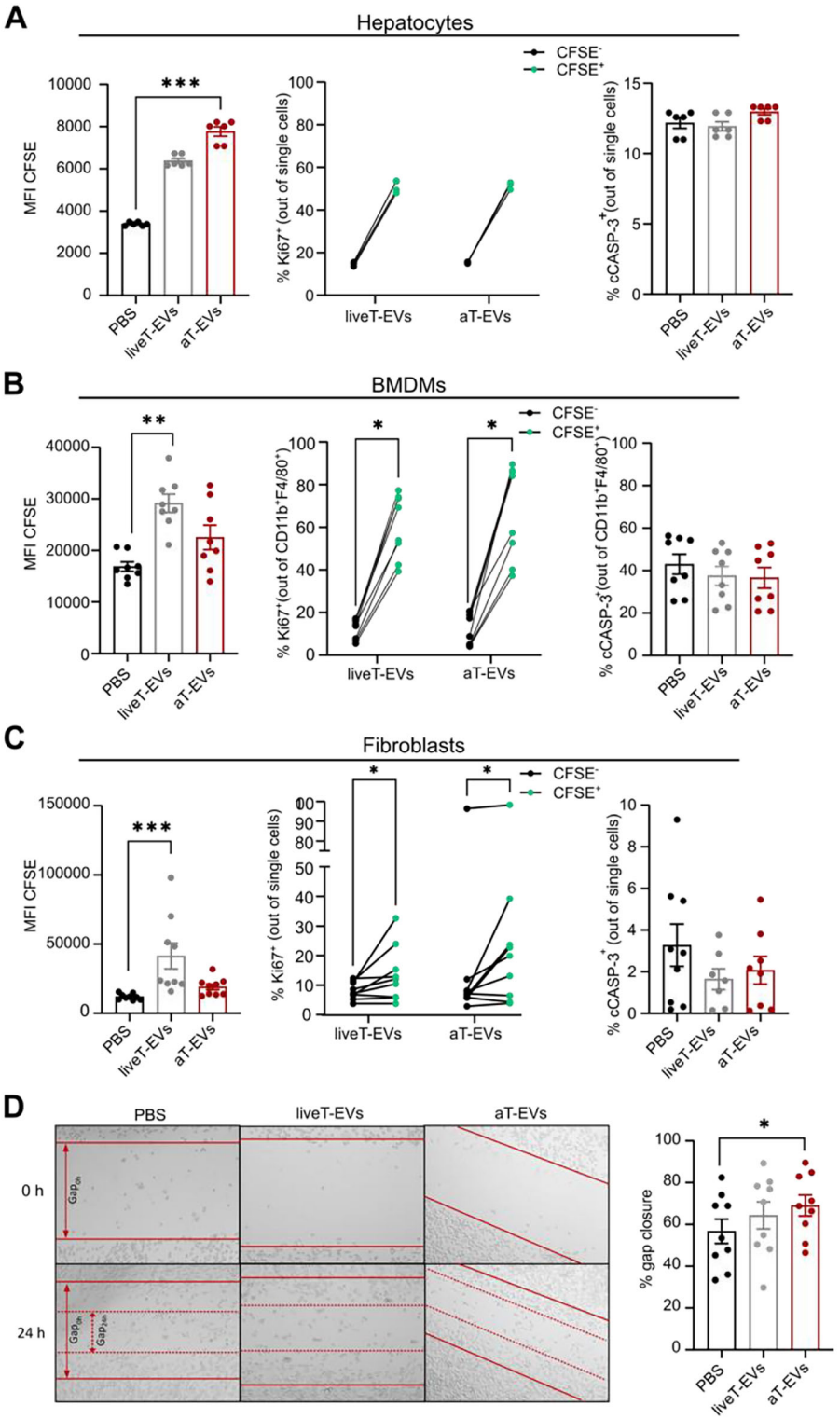

FIGURE 4 | Extracellular vesicles from live and apoptotic T cells differentially impact immune and non-immune cell function. (A) Hepatocytes (HEPA-1-6 cell line), (B) BMDMs (BMDMs) and (C) fibroblasts (WEHI-164 cell line) were incubated in the presence of EVs (a pool of small and large EVs) or PBS (control) for 24 h in vitro. (Left panel) The uptake of CFSE-labelled EVs was analysed by flow cytometry, Kruskal–Wallis test followed by Dunn's multiple comparison test, $^{**}p \leq 0.01$, $^{***}p \leq 0.001$. (Centre panel) The frequency of $Ki67^+$ cells comparing cells that have taken up ($CFSE^+$) or not taken up ($CFSE^-$) CFSE-labelled liveT- or aT-EVs, Multiple Wilcoxon tests, $^{*}p \leq 0.05$, $^{***}p \leq 0.001$. (Right panel) The frequency of $cCASP\text{-}3^+$ target cells 24 h upon incubation in the presence of EVs. Kruskal–Wallis test followed by Dunn's multiple comparison test. (A) $n = 6$; (B) $n = 8$; (C) $n = 9$. Mean ± SEM. (D) Representative images and quantification of scratch closure capacity in fibroblasts (WEHI-164 cell line) upon treatment for 24 h with 20 μg (protein concentration) of liveT- or aT-EVs. Solid red lines indicate the initial position of the wound edge (0 h). Dotted red lines indicate the area covered by migration of the cells into the wound 24 h later. Data are shown as % of gap closure at 24 h compared to 0 h. $n = 9$; Mean ± SEM. Wilcoxon test, $^{*}p \leq 0.05$.

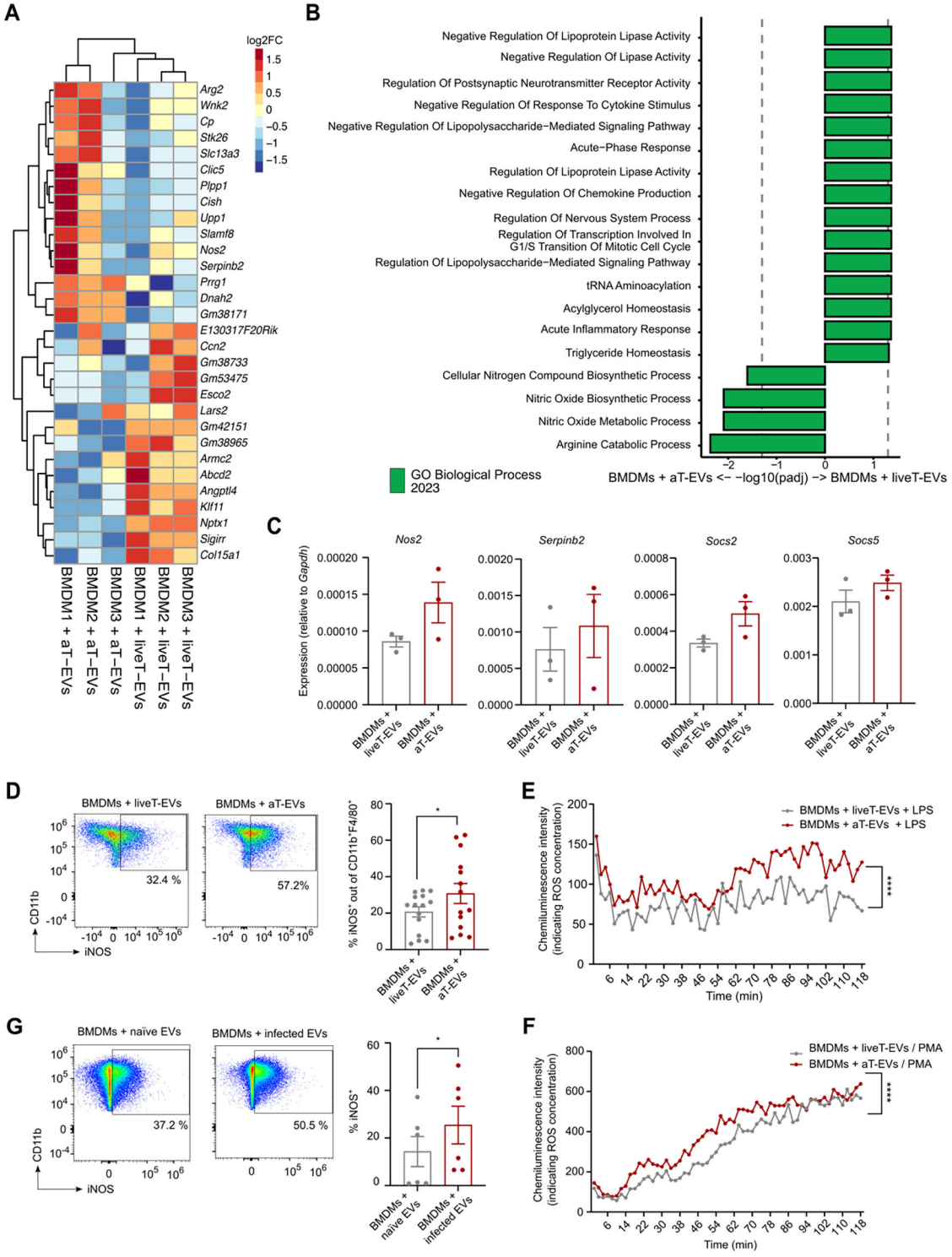

FIGURE 5 | Extracellular vesicles from dying cells trigger Nitric Oxide pathway activation in macrophages. (A) Heatmap visualising the 30 genes most differentially expressed (DE) in BMDMs upon in vitro treatment with liveT- or aT-EVs (a pool of small and large EVs) for 24 h. The displayed genes represent the 15 most highly expressed following liveT-EV treatment and 15 most highly expressed following aT-EV treatment, as detected by bulk-RNA sequencing (log2FC). $n = 3$ biological replicates/condition. (B) GO term analysis of the most DE genes between BMDMs treated with liveT- or aT-EVs. (C) Expression of selected genes from samples in (A), as detected via RT-qPCR. Gene expression is shown as relative to *Gapdh*. $n = 3$; Mean ± SEM. Wilcoxon test. (D) Flow cytometric analysis reporting iNOS expression in $CD11b^{+}F4/80^{+}$ BMDMs 24 h after incubation with liveT- (grey) or aT-EVs (red). $n = 14 – 15$; Mean ± SEM. Wilcoxon test, $^{*}p \leq 0.05$ (E) ROS production by BMDMs activated with LPS and treated with liveT- or aT-EVs. Results are shown as chemiluminescence intensity, measured via Luminol Assay during a 118 min kinetic. Area under the curve was calculated and compared between samples using an unpaired T test, $^{****}p \leq 0.0001$. (F) ROS production by BMDMs activated with PMA and treated with liveT- or aT-EVs. Results are shown as chemiluminescence intensity, measured via Luminol Assay during 118 min kinetic. Area under the curve was calculated

and compared between samples using an unpaired T test, ****$p \leq 0.0001$. (G) Flow cytometric analysis of iNOS expression in CD11b$^+$F4/80$^+$ BMDMs after 48 h of incubation in the presence of liver-derived EVs (100,000 rcf pellet) isolated from naïve (grey) or *S. mansoni*-infected (red) mice, as detected by flow cytometry. $n = 6$; Mean ± SEM. Wilcoxon test, *$p \leq 0.05$.

BMDMs exposed to liveT- or aT-EVs with either LPS or PMA. Stimulation with LPS causes a slower, lower and more sustained increase in ROS production, which is an important immune mechanism in pathogen defence. In contrast, stimulation with PMA is an artificial stimulus leading to a rapid and intense, but transient increase in ROS production (Johann et al. 2006; Swindle et al. 2002). Regardless of the stimulus, treatment of BMDMs with aT-EVs leads to higher levels of ROS production, compared to liveT-EVs, as detected by higher chemiluminescence intensity via a luminol assay (Figure 5E, F). Interestingly, liver-derived EVs isolated from *S. mansoni*-infected livers also induce iNOS protein expression in BMDMs compared with naïve liver-derived EVs (Figure 5G; Figure S12). This observation is consistent with the enrichment in miR-155 in EVs from *S. mansoni*-infected livers compared with naïve counterparts (Sup. Table 1), as miR-155 is associated with the induction of a pro-inflammatory Mφ phenotype characterized by high iNOS expression (Zhang Z. et al. 2022). Importantly, although, in this setting, we detected only minimal amounts of miRNAs derived from *S. mansoni*, we cannot exclude that EVs derived from infected livers also contain EVs from the parasite, which have already been described to affect different aspects of the host immune response (Mossallam et al. 2021). Additionally, our data indicate that activation of the NO pathway is a conserved feature of ApoEVs and of EVs accumulating in the infected liver, likely originating from dying cells. This identifies a previously unappreciated pro-inflammatory function of ApoEVs, in contrast to the anti-inflammatory signature elicited by intact apoptotic cells when sensed by Mφs (Bosurgi et al. 2017; Freire-de-Lima et al. 2006).

4 | Discussion

Due to their ability to deliver proteins and nucleic acids to target cells, EVs function as important intercellular messengers. Their roles vary significantly depending on their cell of origin. Tumour-derived EVs, for example, in several contexts can promote anti-inflammatory Mφ polarisation and thereby tumour progression (Tian et al. 2023), whereas EVs isolated from conditions such as inflammatory bowel disease, acute lung injury, and idiopathic pulmonary fibrosis, can promote disease progression by inducing pro-inflammatory polarisation of Mφs (Tang et al. 2022).

However, whether the fitness of the originating cell influences the characteristics and functions of the released EVs has not been thoroughly investigated. Our results show that the EVs released by cells undergoing apoptosis are distinct from those released by viable cells. In particular, EVs differ in their cargo composition, as apoptotic thymocytes-derived EVs (aT-EVs) are enriched in proteins that are associated with EV biogenesis and cargo packaging involving mainly DNA and RNA binding and processing. This, firstly, suggests that aT-EVs might differ not only in protein, but also in RNA and DNA content compared to liveT-EVs. Secondly, higher abundance of proteins involved in EV biogenesis might hint towards increased EV production during apoptosis, which, in turn, could confirm our observation of higher concentrations of ApoEVs compared to live cells. Caspases are typically activated in response to various cell death stimuli, and their cleavage is a characteristic feature of cells undergoing apoptosis (Cohen 1997). In line with this, aT-EVs are enriched in the apoptosis-specific protein cCASP-3. While the packaging of cCASP-3 in EVs has been described as a mechanism to protect surrounding cells from exposure to cCASP-3 activity (Böing et al. 2013), in our experimental settings, the cCASP-3 does not seem to be delivered to target cells upon uptake. However, the ApoEVs still impact the target cell in a manner distinct from EVs obtained from the live cell counterpart. Herein, we could demonstrate that BMDMs treated with aT-EVs upregulate nitric oxide production pathways compared to BMDMs treated with liveT-EVs on mRNA and protein levels. Interestingly, pathways involved in NO production were found to be most DE in aT-EV-treated BMDMs, suggesting that aT-EVs, via their cargo, may specify their effect on Mφs. This further highlights the significance of EVs for specific and directed cell targeting.

In particular, aT-EVs influence the Mφs capacity to produce ROS, which is known as one of the major pathogen defence mechanisms of pro-inflammatory Mφs (Herb and Schramm 2021). Given the established role of miR-155 in promoting iNOS expression in Mφs (Jablonski et al. 2016) and in driving pro-inflammatory Mφ activation in the context of myocardial infarction (Ge et al. 2021), together with our observation that EVs from *S. mansoni*-infected livers are enriched in miR-155, it is tempting to speculate that miR-155 delivery via EVs contributes to the pro-inflammatory activity of ApoEVs.

The sensing of apoptotic cells, in the context of activated Mφs (such as upon LPS or IL-4 stimulation), has been described by us and others as a key determinant in the induction of an anti-inflammatory or immunosuppressive signature in efferocytic cells (Bosurgi et al. 2017; Fadok et al. 1998; Freire-de-Lima et al. 2006; Moshkovits et al. 2015; Stern et al. 1996; Voll et al. 1997). Moreover, we have previously shown that, in vitro, within an IL-4-enriched environment, conditioned media from apoptotic neutrophils, most likely also containing EVs, is not sufficient to trigger the anti-inflammatory signature typically observed upon direct uptake of apoptotic neutrophils (Liebold et al. 2024). Although obtained from a different in vitro experimental setting, these findings differ from those using enriched EV preparations derived from apoptotic thymocytes and from the effects of those EVs on target Mφs. Based on this, it is tempting to speculate that EVs derived from different cell types may not only carry distinct signals but also be differentially sensed and taken up by Mφs. These possibilities remain to be investigated.

Additionally, our current data suggest that, in contrast to the anti-inflammatory effect on Mφs triggered by the sensing of apoptotic cells themselves, EVs from aT promote a pro-inflammatory polarisation of targeted Mφs, primarily mediated by the activation of NO-related pathways. Pro-inflammatory signalling of Apo-EVs

has been described previously (Berda-Haddad et al. 2011; Schiller et al. 2012), and we hypothesise that selective cargo packaging during EV biogenesis, the engagement of different signalling receptors on target cells, or the influence of the surrounding microenvironment during the EV–target-cell interaction may all contribute to the distinct effects of EVs compared to those of their cells of origin. We also observed a similar induction of iNOS expression when Mφs were treated with EVs isolated from the livers of *S. mansoni*-infected mice. Although the infected liver is enriched in immune cells, some of which undergo apoptosis, we cannot exclude the possibility that EVs released by *S. mansoni* parasites/eggs also contribute to the pool of particles whose characteristics and effects on Mφs are described in this study. Additionally, given the role of *S. mansoni*-derived EVs as regulators of the immune response (Qi et al. 2023; L. Wang et al. 2022; Y. Wang et al. 2022) and as immunising agents in experimental schistosomiasis (Mossallam et al. 2021), it is possible that these parasite-derived EVs contribute to the observed effects on target Mφs, such as the increase in iNOS expression.

EVs provide advantages compared to cells in practical applications, such as their ability to travel longer distances and reach more distant cells, which might help reduce systemic side effects. Additionally, EVs may be further engineered by incorporating specific surface markers or intravesicular cargo. Their specificity and longevity can be enhanced by adding surface molecules, such as don't eat me signals (Kamerkar et al. 2017). The differing features and impacts of EVs originating from live versus apoptotic cells, as described here, represent an additional mechanism to consider when enhancing or tailoring EV effects on target cells in future practical applications. We believe this may be particularly relevant in the context of chronic diseases, such as persistent *S. mansoni* infection, where Mφs with anti-inflammatory features exacerbate tissue pathology by enhancing type 2 immune responses (Nono et al. 2017). Thus, during the chronic phase of infection, rewiring Mφs activation towards a pro-inflammatory state, thereby promoting fibroblast-mediated wound healing and preventing hepatocyte damage, as suggested by our in vitro results and by the effects of aT-EVs injection in *S. mansoni*-infected mice, may be useful to reverse established fibrosis and limit uncontrolled inflammation through the therapeutic transfer of ApoEVs. Nevertheless, future studies are needed to further dissect the contribution of dying cell-derived EVs to target cell function, particularly in vivo, focusing on their cargo composition and the molecular pathways they modulate. Such investigations will be essential to fully define the therapeutic potential of dying cell-derived EVs.

Author Contributions

Stephanie Leyk: conceptualisation, writing – original draft, methodology. **Imke Liebold**: methodology, writing – review and editing. **Clarissa Lanzloth**: methodology, writing – review and editing. **Ulricke Richardt**: methodology. **Johan M. Kux**: writing – review and editing, methodology. **Christoph Kilian**: writing – review and editing. **Manuela Moritz**: writing – review and editing, methodology. **Antonia Gocke**: writing – review and editing, methodology. **Simon Meyer**: writing – review and editing. **Katharina Höhn**: methodology, writing – review and editing. **Barbara Honecker**: writing – review and editing, methodology. **Helmut Haas**: methodology. **Marius Böttcher**: methodology. **Sören Weidemann**: methodology. **Simon Kind**: methodology. **Hartmut Schlüter**: writing – review and editing, methodology. **Nahla Galal Metwally**: methodology, writing – review and editing. **Lorenz Adlung**: methodology. **Pablo J. Sáez**: writing – review and editing, methodology. **Thomas Jacobs**: methodology, writing – review and editing. **Klaus Ruckdeschel**: writing – review and editing. **Lidia Bosurgi**: conceptualisation, funding acquisition, writing – original draft, writing – review and editing.

Acknowledgements

We thank Kristin Hartmann from the Mouse Pathology Core Facility (UKE), Mohsin Shafiq from the Institute for Neuropathology (UKE) for support with the NTA, Johannes Brandi from the Protozoa Immunology Group (BNITM) for advice with spectral flow cytometry, Lara Linnemann from the Helminth Immunology Group (BNITM) for support with the ROS Assay, and all animal caretakers from the BNITM.

Open access funding enabled and organized by Projekt DEAL.

Funding

This work was supported by the Landesforschungsförderung Hamburg under Grant LFF-FV 74-2019 (to K.R. and L.B.), the Deutsche Forschungsgemeinschaft (DFG, BO5198/7-1 to L.B.; 335447717-SFB1328-Project A20 to P.J.S.), Werner Otto Stiftung (04/105 to L.B.), ProExzellenzia Plus (to S.L.), Human Frontier Science Program (HFSP, Grant No. RGP0032/2022 to P.J.S.) https://doi.org/10.52044/HFSP.RGP00322022.pc.gr.153612).

Conflicts of Interest

H.H. is head and owner of *helminGuard*. All the other authors declare that they have no competing interests.

Data Availability Statement

All data needed to evaluate the manuscript are present in the main text or in the supplementary materials. Sequencing files and processed data (mRNA-sequencing of BMDMs treated with EVs from liveT or aT) are available at https://doi.org/10.25592/uhhfdm.18262 and (miRNA-sequencing of EVs from livers of naïve and *S.mansoni*-infected mice) at http://www.ncbi.nlm.nih.gov/bioproject/1416911 with identifier PRJNA1416911. Proteomic data are available via ProteomeXchange with identifier PXD063388.

References

An, P., L. L. Wei, S. Zhao, et al. 2020. "Hepatocyte Mitochondria-derived Danger Signals Directly Activate Hepatic Stellate Cells and Drive Progression of Liver Fibrosis." *Nature Communications* 11, no. 1: 2362. https://doi.org/10.1038/s41467-020-16092-0.

Berda-Haddad, Y., S. Robert, P. Salers, et al. 2011. "Sterile Inflammation of Endothelial Cell-Derived Apoptotic Bodies Is Mediated by Interleukin-1α." *Proceedings of the National Academy of Sciences of the United States of America* 108, no. 51: 20684–20689. https://doi.org/10.1073/pnas.1116848108.

Bilyy, R. O., T. Shkandina, A. Tomin, et al. 2012. "Macrophages Discriminate Glycosylation Patterns of Apoptotic Cell-Derived Microparticles." *Journal of Biological Chemistry* 287, no. 1: 496–503. https://doi.org/10.1074/jbc.M111.273144.

Böing, A. N., J. Stap, C. M. Hau, et al. 2013. "Active Caspase-3 Is Removed From Cells by Release of Caspase-3-Enriched Vesicles." *Biochimica et Biophysica Acta (BBA)—Molecular Cell Research* 1833, no. 8: 1844–1852. https://doi.org/https://doi.org/10.1016/j.bbamcr.2013.03.013.

Bosurgi, L., Y. G. Cao, M. Cabeza-Cabrerizo, et al. 2017. "Macrophage Function in Tissue Repair and Remodeling Requires IL-4 or IL-13 With Apoptotic Cells." *Science* 356, no. 6342: 1072–1076. https://doi.org/10.1126/science.aai8132.

Bratton, D. L., V. A. Fadok, D. A. Richter, J. M. Kailey, L. A. Guthrie, and P. M. Henson. 1997. "Appearance of Phosphatidylserine on Apoptotic Cells Requires Calcium-Mediated Nonspecific Flip-Flop and Is Enhanced by Loss of the Aminophospholipid Translocase." *Journal of Biological Chemistry* 272, no. 42: 26159–26165. https://doi.org/10.1074/jbc.272.42.26159.

Caruso, S., and I. K. H. Poon. 2018. "Apoptotic Cell-Derived Extracellular Vesicles: More than Just Debris." *Frontiers in Immunology* 28:9: 1486. https://doi.org/10.3389/fimmu.2018.01486.

Castanza, A. S., J. M. Recla, D. Eby, H. Thorvaldsdóttir, C. J. Bult, and J. P. Mesirov. 2023. "Extending Support for Mouse Data in the Molecular Signatures Database (MSigDB)." *Nature Methods* 20, no. 11: 1619–1620. https://doi.org/10.1038/s41592-023-02014-7.

Cocca, B. A., A. M. Cline, and M. Z. Radic. 2002. "Blebs and Apoptotic Bodies Are B Cell Autoantigens." *The Journal of Immunology* 169, no. 1: 159–166. https://doi.org/10.4049/jimmunol.169.1.159.

Cohen, G. M. 1997. "Caspases: The Executioners of Apoptosis." *The Biochemical Journal* 326, no. Pt 1: 1–16. https://doi.org/10.1042/bj3260001.

Dannenhaus, T. A., F. Winkelmann, C. Reinholdt, et al. 2024. "Intra-Specific Variations in Schistosoma mansoni and Their Possible Contribution to Inconsistent Virulence and Diverse Clinical Outcomes." *PLoS neglected tropical diseases* 18, no. 10: e0012615. https://doi.org/10.1371/journal.pntd.0012615.

David, J. W., S. M. Wahl, and L. M. Wahl. 1978. "Hepatic Fibrosis in Schistosomiasis: Egg Granulomas Secrete Fibroblast Stimulating Factor in Vitro." *Science* 202, no. 4366: 438–440. https://doi.org/10.1126/science.705337.

Enari, M., H. Sakahira, H. Yokoyama, K. Okawa, A. Iwamatsu, and S. Nagata. 1998. "A Caspase-Activated DNase That Degrades DNA During Apoptosis, and Its Inhibitor ICAD." *Nature* 391, no. 6662: 43–50. https://doi.org/10.1038/34112.

Estaquier, J., M. Marguerite, F. Sahuc, N. Bessis, C. Auriault, and J. C. Ameisen. 1997. "Interleukin-10 – Mediated T Cell Apoptosis During the T Helper Type 2 Cytokine Response in Murine Schistosoma Man-Soni Parasite Infection." *European Cytokine Network* 8, no. 2: 153–160.

Fadok, V. A., D. L. Bratton, A. Konowal, P. W. Freed, J. Y. Westcott, and P. M. Henson. 1998. "Macrophages That Have Ingested Apoptotic Cells in Vitro Inhibit Proinflammatory Cytokine Production Through Autocrine/Paracrine Mechanisms Involving TGF-, PGE2, and PAF." *The Journal of Clinical Investigation* 101, no. 4: 890–898. https://doi.org/10.1172/JCI1112.

Freire-de-Lima, C. G., Q. X. Yi, S. J. Gardai, D. L. Bratton, W. P. Schiemann, and P. M. Henson. 2006. "Apoptotic Cells, Through Transforming Growth Factor-β, Coordinately Induce Anti-Inflammatory and Suppress Pro-Inflammatory Eicosanoid and NO Synthesis in Murine Macrophages." *Journal of Biological Chemistry* 281, no. 50: 38376–38384. https://doi.org/10.1074/jbc.M605146200.

Frey, B., and U. S. Gaipl. 2011. "The Immune Functions of Phosphatidylserine in Membranes of Dying Cells and Microvesicles." *Seminars in Immunopathology* 33, no. 5: 497–516. https://doi.org/10.1007/s00281-010-0228-6.

Ge, X., Q. Meng, L. Wei, et al. 2021. "Myocardial Ischemia-Reperfusion Induced Cardiac Extracellular Vesicles Harbour Proinflammatory Features and Aggravate Heart Injury." *Journal of Extracellular Vesicles* 10, no. 4: e12072. https://doi.org/10.1002/jev2.12072.

Herb, M., and M. Schramm. 2021. "Functions of Ros in Macrophages and Antimicrobial Immunity." *Antioxidants* 10, no. 2: 1–39. https://doi.org/10.3390/antiox10020313.

Ishak, K., A. Baptista, l. Bianchi, et al. 1995. "Histological Grading and Staging of Chronic hepatitis." *Journal of Hepatology* 22, no. 6: 696–699. https://doi.org/10.1016/0168-8278(95)80226-6.

Jablonski, K. A., A. D. Gaudet, S. A. Amici, P. G. Popovich, and M. Guerau-de-Arellano. 2016. "Control of the Inflammatory Macrophage Transcriptional Signature by miR-155." *PLoS ONE* 11, no. 7: e0159724. https://doi.org/10.1371/journal.pone.0159724.

Johann, A. M., A. von Knethen, D. Lindemann, and B. Brüne. 2006. "Recognition of Apoptotic Cells by Macrophages Activates the Peroxisome Proliferator-Activated Receptor-γ and Attenuates the Oxidative Burst." *Cell Death and Differentiation* 13, no. 9: 1533–1540. https://doi.org/10.1038/sj.cdd.4401832.

Kamerkar, S., V. S. Lebleu, H. Sugimoto, et al. 2017. "Exosomes Facilitate Therapeutic Targeting of Oncogenic KRAS in Pancreatic Cancer." *Nature* 546, no. 7659: 498–503. https://doi.org/10.1038/nature22341.

Kerr, J. F. R., A. H. Wyllie, and A. R. Curriet. 1972. "Apoptosis: A Basic Biological Phenomenon With Wide-Ranging Implications in Tissue Kinetics." *Brititsh Journal of Cancer* 26, no. 4: 239–257. https://doi.org/10.1038/bjc.1972.33.

Kisseleva, T., and D. Brenner. 2021. "Molecular and Cellular Mechanisms of Liver Fibrosis and Its Regression." *Nature Reviews Gastroenterology & Hepatology* 18, no. 3: 151–166. https://doi.org/10.1038/s41575-020-00372-7.

Knuhr, K., K. Langhans, S. Nyenhuis, et al. 2018. "Schistosoma mansoni Egg-Released IPSE/Alpha-1 Dampens Inflammatory Cytokine Responses via Basophil Interleukin (IL)-4 and IL-13." *Frontiers in Immunology* 10:9: 2293. https://doi.org/10.3389/fimmu.2018.02293.

Korotkevich, G., V. Sukhov, N. Budin, B. Shpak, M. N. Artyomov, and A. Sergushichev. 2016. "Fast Gene Set Enrichment Analysis." *BioRxiv* 060012. https://doi.org/10.1101/060012.

Liebold, I., A. Al Jawazneh, C. Casar, et al. 2024. "Apoptotic Cell Identity Induces Distinct Functional Responses to IL-4 in Efferocytic Macrophages." *Science* 384, no. 6691: eabo7027. https://doi.org/10.1126/science.abo7027.

Mandal, D., A. Mazumder, P. Das, M. Kundu, and J. Basu. 2005. "Fas-, Caspase 8-, and Caspase 3-Dependent Signaling Regulates the Activity of the Aminophospholipid Translocase and Phosphatidylserine Externalization in Human Erythrocytes." *Journal of Biological Chemistry* 280, no. 47: 39460–39467. https://doi.org/10.1074/jbc.M506928200.

Molehin, A. J. 2020. "Current Understanding of Immunity Against Schistosomiasis: Impact on Vaccine and Drug Development." *Research and Reports in Tropical Medicine* 11: 119–128. https://doi.org/10.2147/rrtm.s274518.

Moshkovits, I., D. Karo-Atar, M. Itan, et al. 2015. "CD300f Associates With IL-4 Receptor α and Amplifies IL-4-Induced Immune Cell Responses." *Proceedings of the National Academy of Sciences of the United States of America* 112, no. 28: 8708–8713. https://doi.org/10.1073/pnas.1507625112.

Mossallam, S. F., I. F. Abou-El-Naga, A. Abdel Bary, E. A. Elmorsy, and R. G. Diab. 2021. "Schistosoma Mansoni Egg-Derived Extracellular Vesicles: A Promising Vaccine Candidate Against Murine Schistosomiasis." *PLoS neglected tropical diseases* 15, no. 10: e0009866. https://doi.org/10.1371/journal.pntd.0009866.

Nono, J. K., H. Ndlovu, N. A. Aziz, T. Mpotje, L. Hlaka, and F. Brombacher. 2017. "Host Regulation of Liver Fibroproliferative Pathology During Experimental Schistosomiasis via Interleukin-4 Receptor Alpha." *PLoS neglected tropical diseases* 11, no. 8: e0005861. https://doi.org/10.1371/journal.pntd.0005861.

Norbury, C. J., and I. D. Hickson. 2001. "Cellular Responses to DNA Damage." *Annual Review of Pharmacology and Toxicology* 41: 367–401. https://doi.org/10.1146/annurev.pharmtox.41.1.367.

Nössing, C., and K. M. Ryan. 2023. "50 years On and Still Very Much Alive: 'Apoptosis: A Basic Biological Phenomenon With Wide-Ranging Implications in Tissue Kinetics'." *British Journal of Cancer* 128, no. 3: 426–431. https://doi.org/10.1038/s41416-022-02020-0.

Pontejo, S. M., and P. M. Murphy. 2021. "Chemokines Act as Phosphatidylserine-Bound 'Find-Me' Signals in Apoptotic Cell Clearance." *PLoS Biology* 19, no. 5: e3001259. https://doi.org/10.1371/journal.pbio.3001259.

Qi, X., Y. Pu, F. Chen, et al. 2023. "Schistosome Egg Antigen Stimulates the Secretion of miR-33-Carrying Extracellular Vesicles From Macrophages to Promote Hepatic Stellate Cell Activation and Liver Fibrosis in Schistosomiasis." *PLoS Neglected Tropical Diseases* 17, no. 5: e0011385. https://doi.org/10.1371/journal.pntd.0011385.

Robbins, P. D., and A. E. Morelli. 2014. "Regulation of Immune Responses by Extracellular Vesicles." *Nature Reviews Immunology* 14, no. 3: 195–208. https://doi.org/10.1038/nri3622.

Rutitzky, L. I., G. A. Mirkin, and M. J. Stadecker. 2003. "Apoptosis by Neglect of CD4 Th Cells in Granulomas: A Novel Effector Mechanism Involved in the Control of Egg-Induced Immunopathology in Murine Schistosomiasis." *Journal of Immunology* 15;171, no. 4: 1859–1867. https://doi.org/10.4049/jimmunol.171.4.1859.

Schiller, M., M. Parcina, P. Heyder, et al. 2012. "Induction of Type I IFN Is a Physiological Immune Reaction to Apoptotic Cell-Derived Membrane Microparticles." *The Journal of Immunology* 189, no. 4: 1747–1756. https://doi.org/10.4049/jimmunol.1100631.

Schilperoort, M., D. Ngai, S. R. Sukka, K. Avrampou, H. Shi, and I. Tabas. 2023. "The role of efferocytosis-fueled macrophage metabolism in the resolution of inflammation." *Immunological Reviews* 319, no. 1: 65–80. https://doi.org/10.1111/imr.13214.

Schwartz, C., and P. G. Fallon. 2018. "Schistosoma "Eggs-Iting" the Host: Granuloma Formation and Egg Excretion." *Frontiers in Immunology* 29:9: 2492. https://doi.org/10.3389/fimmu.2018.02492.

Segawa, K., S. Kurata, Y. Yanagihashi, T. R. Brummelkamp, F. Matsuda, and S. Nagata. 2014. "Caspase-Mediated Cleavage of Phospholipid Flippase for Apoptotic Phosphatidylserine Exposure." *Science* 344, no. 6188: 1164–1168. https://doi.org/10.1126/science.1252809.

Silveira, A. M. S., G. Gazzinelli, L. F. Alves-Oliveira, et al. 2004. "Human Schistosomiasis Mansoni: Intensity of Infection Differentially Affects the Production of Interleukin-10, Interferon-γ and Interleukin-13 by Soluble Egg Antigen or Adult Worm Antigen Stimulated Cultures." *Transactions of The Royal Society of Tropical Medicine and Hygiene* 98, no. 9: 514–519. https://doi.org/10.1016/j.trstmh.2003.11.009.

Stern, M., J. Savill, and C. Hasletf. 1996. "Human Monocyte-Derived Macrophage Phagocytosis of Senescent Eosinophils Undergoing Apoptosis Mediation by avf3/CD36/Thrombospondin Recognition Mechanism and Lack of Phlogistic Response." *In American Journal of Pathology* 149, no. 3: 911–921.

Su, T. 2019. "Risk of Liver Fibrosis Beyond a Normal Alanine Aminotransferase Level." *Advances in Digestive Medicine* 6, no. 1: 1–2. https://doi.org/10.1002/aid2.13120.

Subramanian, A., P. Tamayo, V. K. Mootha, et al. 2005. "Gene Set Enrichment Analysis: A Knowledge-Based Approach for Interpreting Genome-Wide Expression Profiles." *Proceedings National Academy of Science USA* 102, no. 43: 15545–15550. https://doi.org/10.1073/pnas.0506580102.

Sui, B., R. Wang, C. Chen, et al. 2021. "Apoptotic Extracellular Vesicles (ApoEVs) Safeguard Liver Homeostasis and Regeneration via Assembling an ApoEV-Golgi Organelle." *BioRxiv* 432630. https://doi.org/10.1101/2021.02.24.432630.

Schumann, Y., A. Gocke, and J. E. Neumann. 2025. "Computational Methods for Data Integration and Imputation of Missing Values in *Omics* Datasets." *Proteomics* 25: e202400100. https://doi.org/10.1002/pmic.202400100.

Sun, J., L. J. Druhan, and J. L. Zweier. 2010. "Reactive Oxygen and Nitrogen Species Regulate Inducible Nitric Oxide Synthase Function Shifting the Balance of Nitric Oxide and Superoxide Production." *Archives of Biochemistry and Biophysics* 494, no. 2: 130–137. https://doi.org/10.1016/j.abb.2009.11.019.

Swindle, E. J., J. A. Hunt, and J. W. Coleman. 2002. "A Comparison of Reactive Oxygen Species Generation by Rat Peritoneal Macrophages and Mast Cells Using the Highly Sensitive Real-Time Chemiluminescent Probe Pholasin: Inhibition of Antigen-Induced Mast Cell Degranulation by Macrophage-Derived Hydrogen Peroxide." *Journal of Immunology* 169, no. 10: 5866–5873. https://doi.org/10.4049/jimmunol.169.10.5866.

Tang, D., F. Cao, C. Yan, et al. 2022. "Extracellular Vesicle/Macrophage Axis: Potential Targets for Inflammatory Disease Intervention." *Frontiers in Immunology* 13: 705472. https://doi.org/10.3389/fimmu.2022.705472.

Ti, D., H. Hao, C. Tong, et al. 2015. "LPS-preconditioned Mesenchymal Stromal Cells Modify Macrophage Polarization for Resolution of Chronic Inflammation via Exosome-shuttled Let-7b." *Journal of Translational Medicine* 13, no. 1: 308. https://doi.org/10.1186/s12967-015-0642-6.

Tian, J. W., H. J. Zhang, S. Y. Li, Y. L. Guo, G. Chen, and Z. L. Yu. 2023. "Tumor Cell-Derived Extracellular Vesicles in Modulating Phenotypes and Immune Functions of Macrophages: Mechanisms and Therapeutic Applications." *Journal of Cancer* 14, no. 8: 1321–1334. https://doi.org/10.7150/jca.84632.

Tyanova, S., R. Albrechtsen, P. Kronqvist, J. Cox, M. Mann, and T. Geiger. 2016. "Proteomic Maps of Breast Cancer Subtypes." *Nature Communications* 7: 10259. https://doi.org/10.1038/ncomms10259.

Tyanova, S., T. Temu, P. Sinitcyn, et al. 2016. "The Perseus Computational Platform for Comprehensive Analysis of (Prote)Omics Data." *Nature Methods* 13, no. 9: 731–740. https://doi.org/10.1038/nmeth.3901.

van Niel, G., G. D'Angelo, and G. Raposo. 2018. "Shedding Light on the Cell Biology of Extracellular Vesicles." *Nature Reviews Molecular Cell Biology* 19, no. 4: 213–228. https://doi.org/10.1038/nrm.2017.125.

Voll, R. E., M. Herrmann, E. A. Roth, C. Stach, J. R. Kalden, and I. Girkontaite. 1997. "Immunosuppressive Effects of Apoptotic Cells." *Nature* 390, no. 6658: 350–351. https://doi.org/10.1038/37022.

Wahlgren, J., T. D. L. Karlson, P. Glader, E. Telemo, and H. Valadi. 2012. "Activated Human T Cells Secrete Exosomes That Participate in IL-2 Mediated Immune Response Signaling." *PLoS ONE* 7, no. 11: e49723. https://doi.org/10.1371/journal.pone.0049723.

Wang, L., Z. Zhu, Y. Liao, et al. 2022. "Host Liver-Derived Extracellular Vesicles Deliver miR-142a-3p Induces Neutrophil Extracellular Traps via Targeting WASL to Block the Development of Schistosoma Japonicum." *Molecular Therapy* 30, no. 5: 2092–2107. https://doi.org/10.1016/j.ymthe.2022.03.016.

Wang, Y., W. Gong, H. Zhou, et al. 2022. "A Novel miRNA From Egg-Derived Exosomes of Schistosoma Japonicum Promotes Liver Fibrosis in Murine Schistosomiasis." *Frontiers in Immunology* 27, no. 13: 860807. https://doi.org/10.3389/fimmu.2022.860807.

Yarana, C., H. Thompson, L. Chaiswing, et al. 2019. "Extracellular Vesicle-Mediated Macrophage Activation: An Insight Into the Mechanism of Thioredoxin-Mediated Immune Activation." *Redox Biology* 26: 101237. https://doi.org/10.1016/j.redox.2019.101237.

Zhang, S., S. Weinberg, M. DeBerge, et al. 2019. "Efferocytosis Fuels Requirements of Fatty Acid Oxidation and the Electron Transport Chain to Polarize Macrophages for Tissue Repair." *Cell Metabolism* 29, no. 2: 443–456.e5. https://doi.org/10.1016/j.cmet.2018.12.004.

Zhang, Z., H. Chen, L. Zhou, C. Li, G. Lu, and L. Wang. 2022. "Macrophage-derived exosomal miRNA-155 promotes tubular injury in ischemia-induced acute kidney injury." *International Journal of Molecular Medicine* 50, no. 3: 5172. https://doi.org/10.3892/ijmm.2022.5172.

Zhao, K., Z. Huang, H. Lu, J. Zhou, and T. Wei. 2010. "Induction of Inducible Nitric Oxide Synthase Increases the Production of Reactive Oxygen Species in RAW264.7 Macrophages." *Bioscience Reports* 30, no. 4: 233–241. https://doi.org/10.1042/BSR20090048.

Supporting Information

Additional supporting information can be found online in the Supporting Information section.

Supplementary Materials: jex270115-sup-0001-SuppMat.docx